# PLAXIS

## LIQUEFACTION MODEL

**Appropriation**
**Elaboration**
**Implementation**
**Verification**

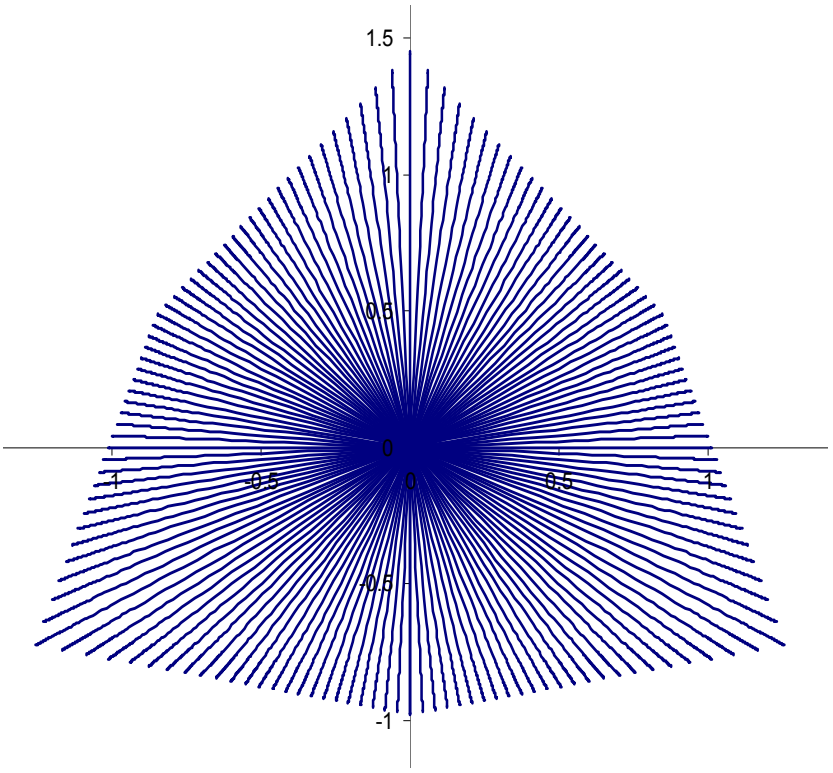


## Report No. 1

**By Anteneh Biru Tsegaye**
(MSc.)

Feb. 2010

# LIQUEFACTION MODEL (UBC3D)

## Report

**Anteneh Biru Tsegaye**

**Plaxis B.V. 2010**
**Delft, The Netherlands**

# Declaration

**This research has been done at Plaxis B.V. from Oct. 2009-Feb. 2010. The name UBC2D is used for the UBC sand model before this implementation (Formulated and implemented in FLAC by Byrne, et al). In this research, the various elastoplastic functions used by the UBC2D model are used. Where necessary, changes are made to a few of the functions. The current implementation (in Plaxis) is fully implicit 3D implementation. A distinction is made by calling the current model as UBC3D (or sometimes Plaxis Liquefaction model-PLM) in the different parts of the document. These names are introduced solely for differentiation.**

**Ir. Anteneh Biru Tsegaye**
**Feb 2010**
**Delft, The Netherlands**

**Table of Contents**

**Page No.**

## List of Figures

**Page No.**

## List of Tables

**Page No.**

## 1. Development of a Liquefaction Model

Background:

The main functions of an elastoplastic model are a yield function, plastic potential function, hardening rule, softening rule, and flow rule. The functions can be formulated in any appropriate way. In this section we select functions (from available elastoplastic models) to develop a simple liquefaction model. The idea of this project has been to implement the UBCSAND model in Plaxis. The UBC SAND model is a simple 2D model developed specially for prediction of liquefaction behavior of sand. Besides its simplicity, the model has been verified in various applications related to liquefaction. Most of the elastoplastic functions in this model are already existing functions in literatures of soil mechanics. Special feature of the model is perhaps the hardening rule, which is a hyperbolic law relating the increment in mobilized friction angle with the plastic shear strain. The original 2D model uses a Mohr-Coulomb yield function and a corresponding non associated plastic potential function. The flow rule is based on the well known Rowe's stress dilatancy formulation with a modification. In the new model, primarily based on the elastoplastic functions mentioned thus far a generalized 3D formulation has been considered. The new model uses the Mohr-Coulomb yield condition in a generalized stress space. The use of non associated plastic potential based on the same function as the yield function (with mobilized friction angle replaced by mobilized dilatancy angle) has been found to introduce non-coaxiality between the stress and the strain in the deviatoric plane. Hence a plastic potential function based on Drucker-Pragers's function has been used which maintains the assumption of stress-strain coaxiality in the deviatoric plane for a stress path beginning from an isotropic stress state. The model has been developed and implemented in such a way various other functions can be easily integrated. The flow rule used by Byrne, et al. in the UBC sand model is a fair estimation of the Rowe's stress dilatancy rule. For mobilized friction angle bellow the critical friction angle, the flow rule is less contractive than Rowe's and above the critical friction angle; the flow rule is more contractive than Rowe's. While the flow rule reduces the strong contractive sense at lower mobilized friction angles and generally for contractive samples, it reduces the effect of dilatancy angle above the critical state friction angle. To reduce this limitation, the modified flow rule can be used for a mobilized friction angle bellow the critical state friction angle and the exact Rowe's formulation above the critical state friction angle. The unloading –reloading criteria in a 3D is relatively complicated than a 2D. In this model, a simple procedure based on the mobilized friction angle is used to model responses for load reversal and change of direction. In general, the model is able to reproduce various stress-strain paths under different conditions. Its simplicity in the formulation as well as the use of only already used parameters would make it a good candidate for modeling the behavior of granular materials.

## 1.1 Basic elastoplastic functions

### 1.1.1 Yield function

In this model, the well known Mohr-Coulomb yield surface has been used. The yield function for the Mohr-Coulomb yield surface involves the maximum and the minimum stress components in the principal stress space. For a three dimensional problem, there are three principal stresses. The principal stresses can be sorted in sequence as $\sigma_{\min} \le \sigma_{\text{int}} \le \sigma_{\max}$. There are various ways to construct a generalized 3D yield surface from the combination of these principal stresses. Each principal stress has its own unique direction in a Cartesian stress space. Hence, $\sigma_1, \sigma_2, \sigma_3$ (not sorted) are directed along the corresponding Cartesian unit eigenvectors $\boldsymbol{p}_1$, $\boldsymbol{p}_2$, $\boldsymbol{p}_3$ respectively. The Mohr-Coulomb yield criterion can therefore be constructed in such a way each stress is directed along its unique direction. This leads to the conception of combination of any two from the three, $c(2,3) = 6$ possible cases with a possibility one direction to accommodate the maximum and the minimum and the intermediate stress twice. The case is illustrated in Table 1

Table 1: The six possibilities in generalized principal stress space

| Case | $\sigma_1$ | $\sigma_2$ | $\sigma_3$ |
|---|---|---|---|
| 1 | $\sigma_{\max}$ | $\sigma_{\min}$ | $\sigma_{\text{int}}$ |
| 2 | $\sigma_{\max}$ | $\sigma_{\text{int}}$ | $\sigma_{\min}$ |
| 3 | $\sigma_{\text{int}}$ | $\sigma_{\max}$ | $\sigma_{\min}$ |
| 4 | $\sigma_{\min}$ | $\sigma_{\max}$ | $\sigma_{\text{int}}$ |
| 5 | $\sigma_{\min}$ | $\sigma_{\text{int}}$ | $\sigma_{\max}$ |
| 6 | $\sigma_{\text{int}}$ | $\sigma_{\min}$ | $\sigma_{\max}$ |

For the six cases, a unique Mohr-Coulomb yield criterion can be defined in such a way:

$$f_m = \frac{\sigma_{\max} - \sigma_{\min}}{2} - \left( \frac{\sigma_{\max} + \sigma_{\min}}{2} + c \cot \varphi_p \right) \sin \varphi_m \qquad (1.1)$$

The intermediate stress state does not influence the Mohr-Coulomb yield criterion. The planes defined by the six cases can be visualized in Figure 1.1.

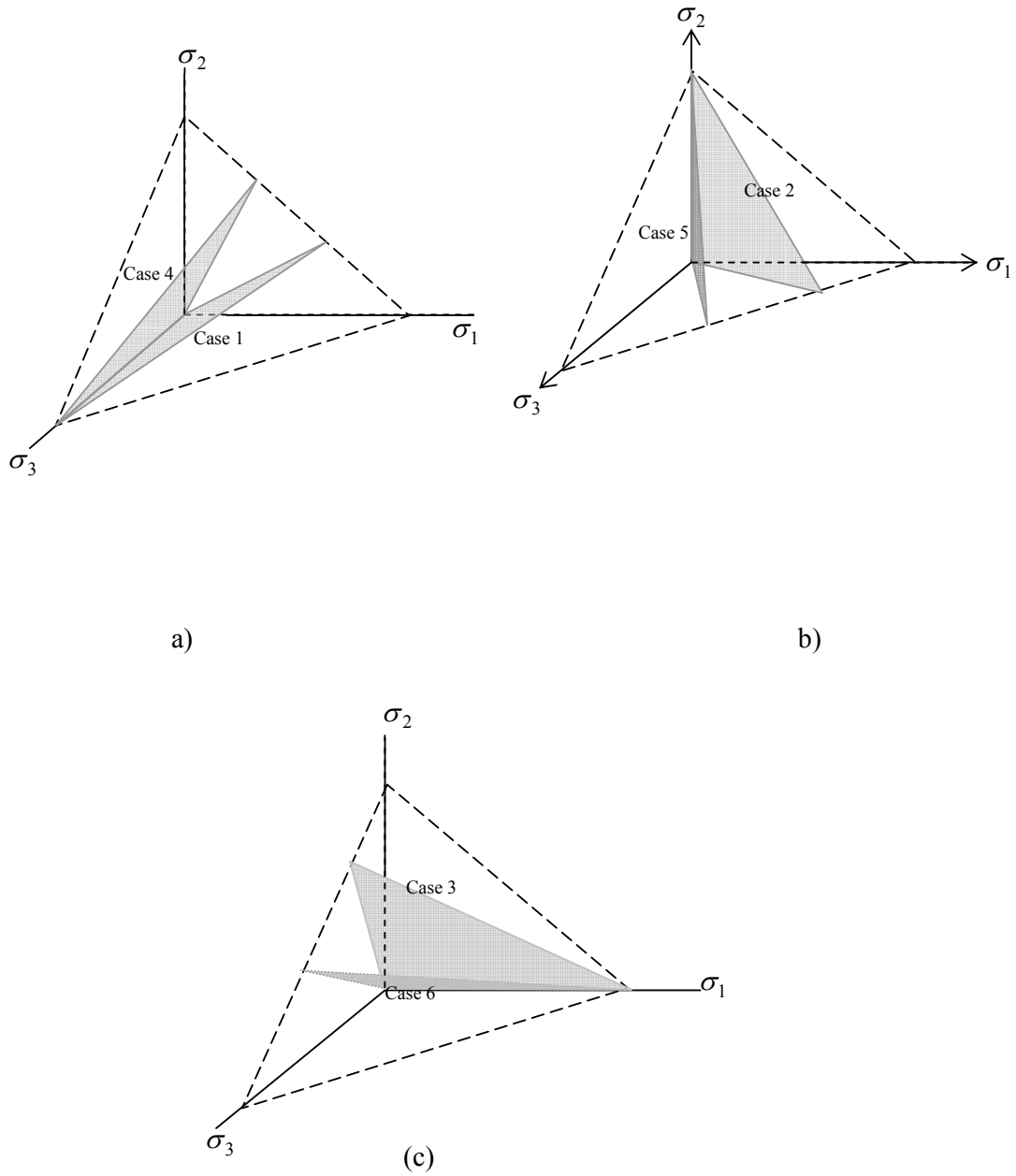


Figure 1. 1 Illustration of the plane yield surfaces for cases: a) 1 and 4 b) c) d) of the Mohr-Coulomb model for zero cohesion $c = 0$ in principal stress space.

When all the 6 planes are combined in one figure and only the part with $\sigma_{min} \le \sigma_{int} \le \sigma_{max}$ is shown, a general 3D surface of the Mohr-Coulomb criterion is obtained (Figure 1.2).

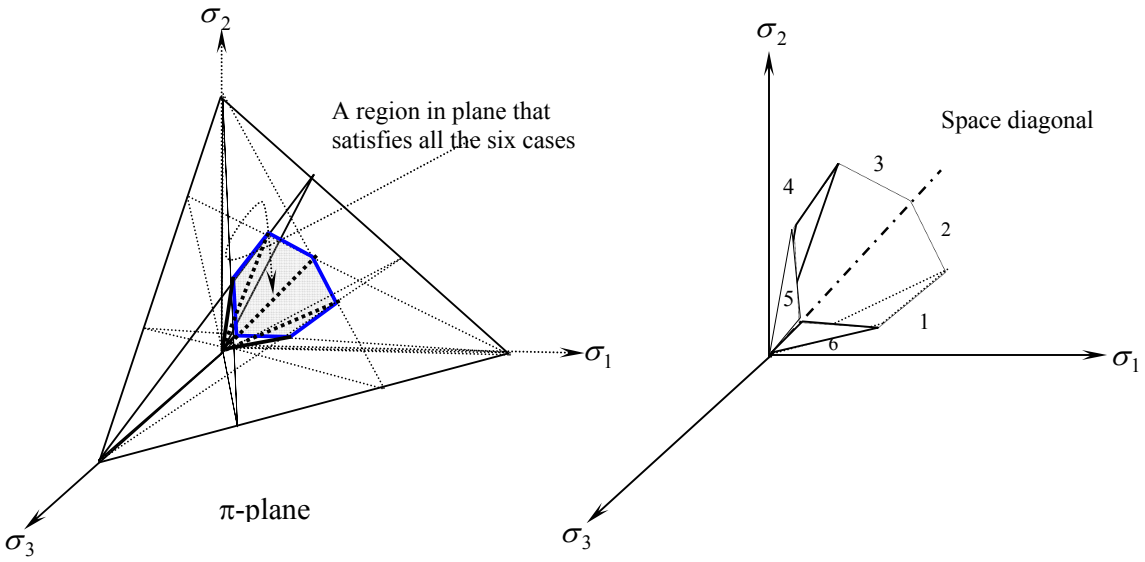


Figure 1.2: (general) The six arrangements of the minimum, intermediate and maximum principal stresses with respect to the principal direction of principal stresses $\sigma_1$, $\sigma_2$ and $\sigma_3$ as specified by their eigenvectors $p_1$, $p_2$, $p_3$.

The projection of the Mohr-Coulomb yield surface in a deviatoric plane is therefore as shown in Figure 1.3:

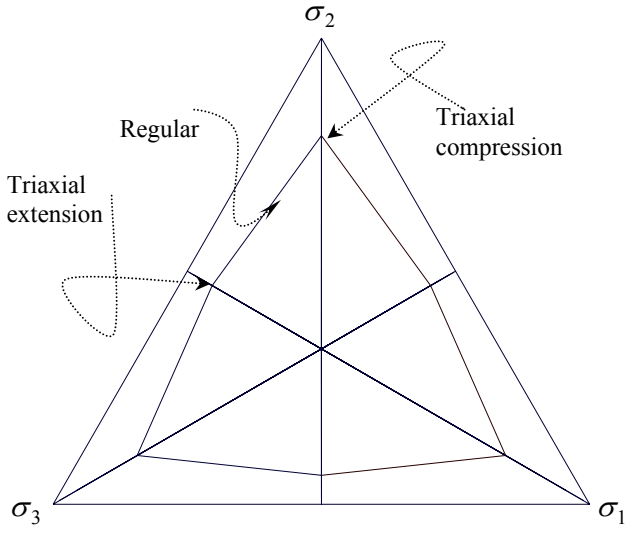


Figure 1.3: Projection of the Mohr-Coulomb yield criterion in $\pi$ plane

As shown in Figure 1.3 six sectors define the Mohr-Coulomb yield surface. Each of the sectors is defined by a regular surface and intersection plane with the neighboring sector. The intersections define states of triaxial compression and triaxial extension. The ridges are discontinuities which need special attention during numerical implementation.

Given the general stress tensor, the principal stresses (eigenvalues) and their corresponding directions (eigenvectors) are obtained by solving the eigenvalue problem given as:

$$\left(\sigma_{ij} - \lambda^{(k)}\delta_{ij}\right) p_j^{(k)} \tag{1.2}$$

Where $\lambda^{(k)}$ are the eigenvalues of the stress tensor and $p_j^{(k)}$ are the eigenvectors which define the direction of each eigenvalue (principal stress). The principal stresses $\sigma_k = \lambda^{(k)}$ are obtained solving:

$$\det\left(\sigma_{ij} - \lambda^{(k)}\delta_{ij}\right) = 0 \tag{1.3}$$

Once the eigenvalues and the eigen vectors are obtained, the principal stresses should be sorted in such a way, $\sigma_1 \geq \sigma_2 \geq \sigma_3$. The indices 1, 2 and 3 do not represent the actual indices obtained in equation (1.2). To know in what region of the $\pi$ plane we need to keep track of the original directions before the sorting and hence amend the eigenvectors accordingly.

After the sorting we obtain sorted principal stresses in such a way $\sigma_1 = \sigma_{\max}$, $\sigma_2 = \sigma_{\text{int}}$ and $\sigma_3 = \sigma_{\min}$. This is numerically done using a subroutine called **PrnSig**.

After the sorting, the yield function can be defined based on the maximum and the minimum principal stresses according to equation (1.1). As long as the six functions are consistently used, the resulting value should fall on the Mohr-coulomb surface.

### 1.1.2 Plastic Hardening

In elasto-plastic modeling hardening law governs the amount of plastic strain (irrecoverable deformation) as a result of mobilization of the yield surface in stress space. There are various hardening laws. Herein the hardening law used in the UBC2D sand model is utilized (with extension for a 3D implementation).

According to the Mohr-Coulomb criterion, the sine of the mobilized friction angle is given as :

$$\sin\varphi_m = \frac{q_m}{p_m} \tag{1.4}$$

Where $q_m = \frac{\sigma_{\max} - \sigma_{\min}}{2}$; $p_m = \frac{\sigma_{\max} + \sigma_{\min}}{2}$

The hardening rule according to Byrne, et al relates the increment of the sine of the mobilized friction angle to the plastic shear strain increment according to:

$$d\sin\varphi_m = \frac{G_i^p}{p_m}\left(1 - \frac{\sin\varphi_m}{\sin\varphi_p} R_f\right)^2 d\gamma^p \tag{1.5}$$

$$G_i^p = k_G^p \left(\frac{p_m}{p_A}\right)^{np} p_A \tag{1.6}$$

The hardening rule considered in this model is generally written as:

$$d\sin\varphi_m = 1.5 k_G^p \left(\frac{p}{p_A}\right)^{np} \frac{p_A}{p_m}\left(1 - \frac{\sin\varphi_m}{\sin\varphi_p} R_f\right)^2 d\lambda \tag{1.7}$$

Where $k_G^p$ is the plastic shear modulus number, $np$ is model parameter for nonlinearity of stiffness dependency of the plastic shear modulus, $p$ is the mean normal stress , $p_A$ is the atmospheric pressure in stress units and $d\lambda$ is the plastic strain increment multiplier.

### 1.1.3 Plastic Potential function

The plastic potential function specifies the direction of the plastic strain increment during the return mapping. Softening problems such as related to liquefaction type deformations require non associated flow rule.

In 2D the yield function is defined by a line. Hence, the plastic potential function can be the same as the yield function with the mobilized friction angle replaced by mobilized dilatancy angle.

In this model we selected the Drucker-Prager type plastic potential function. This function ensures a radial return without complication.

$$g = q - \frac{6\sin\psi_m}{3 - \sin\psi_m}(p + c\cot\varphi_p) \tag{1.8}$$

$g$ is a cone surface passing through triaxial compression points and is basically independent of Lode's angle $\theta_L$ :

$$q = \sqrt{\frac{1}{2}\left\{\left(\sigma_1 - \sigma_2\right)^2 + \left(\sigma_2 - \sigma_3\right)^2 + \left(\sigma_1 - \sigma_3\right)^2\right\}} \tag{1.9}$$

$$p = -\frac{\sigma_1 + \sigma_2 + \sigma_3}{3} \tag{1.10}$$

### 1.1.4 Flow rule

The flow rule enables to relate the plastic shear strain to accumulation of plastic volumetric strain. In this model we used the well known Rowe's stress dilatancy relation.

$$d\varepsilon_v^p = \sin\psi_m d\gamma^p \tag{1.11}$$

$$\sin\psi_m = \sin\varphi_m - \sin\varphi_{cv} \tag{1.12}$$

Where $d\varepsilon_v^p$ is the plastic volumetric strain increment and $\varphi_{cv}$ is the constant volume friction angle.

Note:- Rowe's stress dilatancy when exactly derived is given as $\sin\psi_m = \left(\sin\varphi_m - \sin\varphi_{cv}\right)/\left(1 - \sin\varphi_m.\sin\varphi_{cv}\right)$. Hence the relation given in equation (1.12) is a simplified version as used in the UBC sand model.

This model is a relatively simple model, and a first version, hence various complications are not considered such as drained softening, cap and so on.

### 1.1.5 Tension cut-off

In this model a yield function for tension cut-off is defined based on the minimum principal stress, which is given as:

$$f_t = \sigma_t - \sigma_3 \tag{13}$$

Where $\sigma_t$ is the User defined tension cut-off and $\sigma_3$ is the minimum principal stress after sorting.

### 1.1.6 Summary of functions for the Plaxis Liquefaction Model (UBC3D)

The various elastoplastic functions used in the Plaxis liquefaction model are listed bellow.

1. Elastic stiffness tensor

$$D_{ijkl} = \left( K - \frac{2}{3} G \right) \delta_{ij} \delta_{kl} + 2G \delta_{ik} \delta_{jl} \tag{1.14}$$

$$K = K_{ref} \left( \frac{p}{p_A} \right)^{me} \text{ and } G = G_{ref} \left( \frac{p}{p_A} \right)^{ne} \tag{1.15}$$

Where, $K_{ref}$ and $G_{ref}$ are the bulk modulus and the shear modulus at reference mean normal stress $p_{ref}$ and $ne$ & $me$ are parameters that take into account the nonlinear stress dependency of stiffness. In most literature, $p_{ref}$ is taken at atmospheric pressure $p_a = 100kPa$ .

1. Yield Functions

$$f_m = \frac{\sigma_1 - \sigma_3}{2} - \left( \frac{\sigma_1 + \sigma_3}{2} + c \cot \varphi_p \right) \sin \varphi_m \tag{1.16}$$

$$f_t = \sigma_t - \sigma_3 \tag{1.17}$$

2. Plastic potential functions

$$g_m = q - \frac{6 \sin \psi_m}{3 - \sin \psi_m} (p + c \cot \varphi_p) \tag{1.18}$$

$$g_t = \sigma_t - \sigma_3 \tag{1.19}$$

3. Mobilized dilatancy angle (Rowe as used in the UBC sand model)

$$\sin \psi_m = \sin \varphi_m - \sin \varphi_{cv} \tag{1.20}$$

4. Hardening law

$$d \sin \varphi_m = 1.5 k_G^p \left( \frac{p}{p_A} \right)^{np} \frac{p_A}{p_m} \left( 1 - \frac{\sin \varphi_m}{\sin \varphi_p} R_f \right)^2 d\lambda \tag{1.21}$$

[LEFT BLANK]

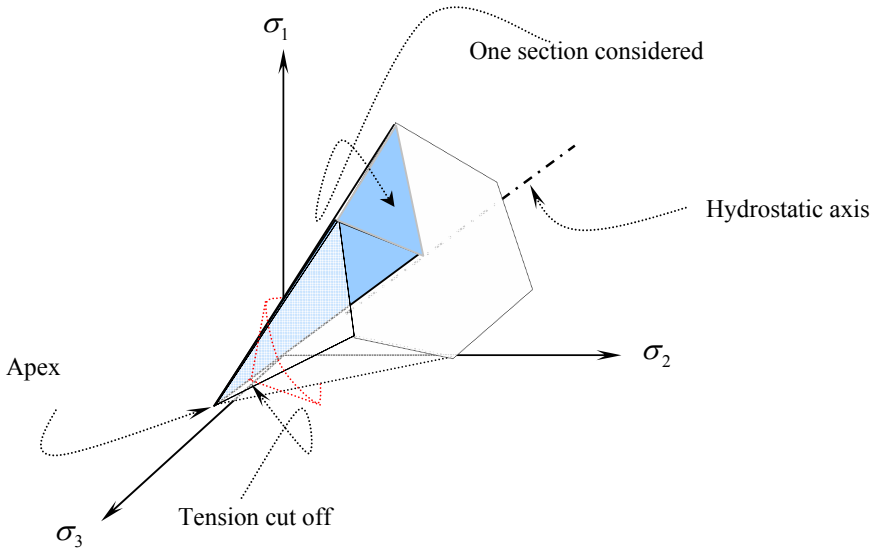


Figure 1.4: The Mohr-Coulomb yield surface and the representative sector surface

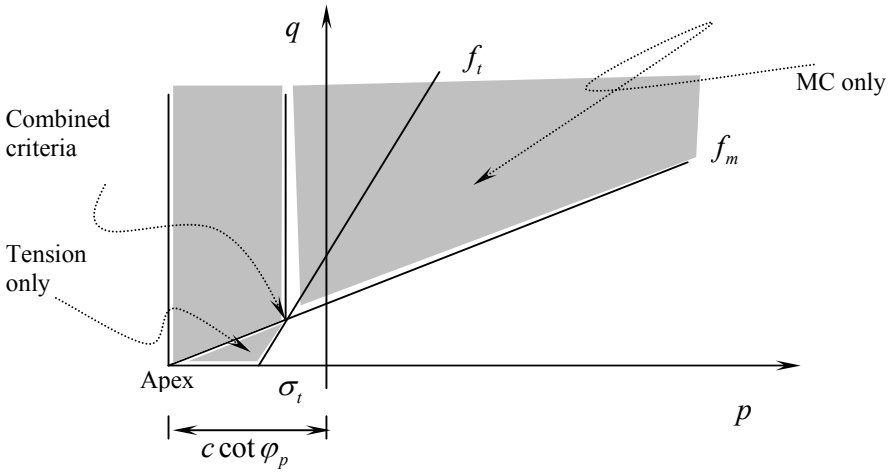


Figure 1.5: Schematization of the yield lines in $p-q$ plane

[LEFT BLANK]

**Relevant Literatures**


1. Michael H Beaty and Peter Byrne. 2007. Liquefaction and deformation analysis using a total stress approach. *Journal of Geotechnical and Geoenvironmental Engineering,* Vol. 134, No. 8

2. Beaty, M. & Byrne, P.M. 1998. An effective stress model for predicting liquefaction behaviour of sand. Geotechnical Earthquake Engineering and Soil Dynamics III. Edited by P. Dakoulas, M. Yegian, and R Holtz (eds.), ASCE, Geo-technical Special Publication 75 (1): 766-777.

3. Byrne, P.M., Park, S.-S., Beaty, M., Sharp, M., Gonzalez, L. & Abdoun, T. 2004. Numerical modeling of liquefaction and comparison with centrifuge tests. Can. Geotech. Journal, Vol. 41, No. 2: 193-211.

4. Byrne, P.M., Roy, D., Campanella, R.G. & Hughes, J. 1995. Predicting liquefaction response of granular soils from pressuremeter tests. ASCE National Convention, San Diego, Oct. 23-27, ASCE, Geotechnical Special Publication 56: 122-135.
5. Puebla, H., Byrne, P.M. & Phillips, R. 1997. Analysis of CANLEX liquefaction embankments: prototype and centri-fuge models. Can. Geotech. Journal, Vol. 34, No. 5: 641-657.

6. Duncan, J.M., Byrne, P.M., Wong, K.S., and Marby, P. 1980. Strength, stress-strain and bulk modulus parameters for finite element analyses of stresses and movements in soil masses. University of California, Berkeley, Report UCB/GT/80–01.

7. Rowe, P.W. 1962. The stress-dilatancy relation for static equilibrium of an assembly of particles in contact. Proceedings of the Royal Society of London, Mathematical and Physical Sciences, Series A, **269**: 500–557.

8. Drucker, D.C. and W. Prager, Soil mechanics and plastic analysis for limit design. Quart. Appl. Math., 1952. **9**: p. 381-389.

9. Wang, Y.-J., J.-H. Yin, and C.F. Lee, The infuence of a non-associated fow rule on the calculation of the factor of safety of soil slopes. Int. J. Numer. Anal. Meth. Geomech, 2001. **25**: p. 1351-1359.

10. Vermeer, P.A. and R.d. Borst, Non associated-Plasticity for soils, concerete and rock. HERON, 1984. **29**(3).

11. Lade, P.V., Instability of granular materials, in Physics and Mechanics of liquefaction. 2002.

12. Tsegaye, A.B. 2009. Evaluation of material models for liquefaction. MSc. Thesis. Department of Geotechnical Engineering. Delft University of Technology, Netherlands

13. M.D.Bolton, The strength and dilatancy of sands. Geotechnique, 1986. **36**(1): p. 65-78.

14. Brinkgreve, R.B.J & W. Broere (eds). 2004. Plaxis 2D-Version 8. Delft University of Technology & Plaxis b.v., The Netherlands.

# Appendices

## 1. List of model parameters

Table 2: List of parameters

| No. | Parameter Name | Symbol | unit | Method of determination | Default value |
|---|---|---|---|---|---|
| 1 | Elastic shear modulus number | $k_G^e$ | - | Empirical, fitting | |
| 2 | Elastic Bulk modulus number | $k_B^e$ | - | Empirical, fitting | |
| 3 | Plastic shear modulus number | $k_G^p$ | - | Empirical, fitting | |
| 4 | Elastic shear modulus index | $ne$ | - | Empirical, fitting | 0.5 |
| 5 | Elastic Bulk modulus index | $me$ | - | Empirical, fitting | 0.5 |
| 6 | Plastic shear modulus index | $np$ | - | Empirical, fitting | 0.5 |
| 7 | Constant volume friction angle | $\varphi_{cv}$ | [$^0$] | Drained Triaxial compression | |
| 8 | Peak friction angle | $\varphi_p$ | [$^0$] | Drained Triaxial Compression | |
| 9 | Cohesion | $c$ | [kPa] | Drained Triaxial Compression | 0 |
| 10 | Failure Ratio | $R_f$ | - | - | 0.95 |
| 11 | Tension cut-off | $\sigma_t$ | [kPa] | - | 0.0 |

## 2. Illustration, Verification and validation

### 2.1 Mobilization of the pi-plane during isochoric monotonic and cyclic loading.

For verification of the return mapping, mobilization of stress paths in the $\pi$ plane during isochoric monotonic and cyclic deformation has been compared to the hypoplasticity soil model.

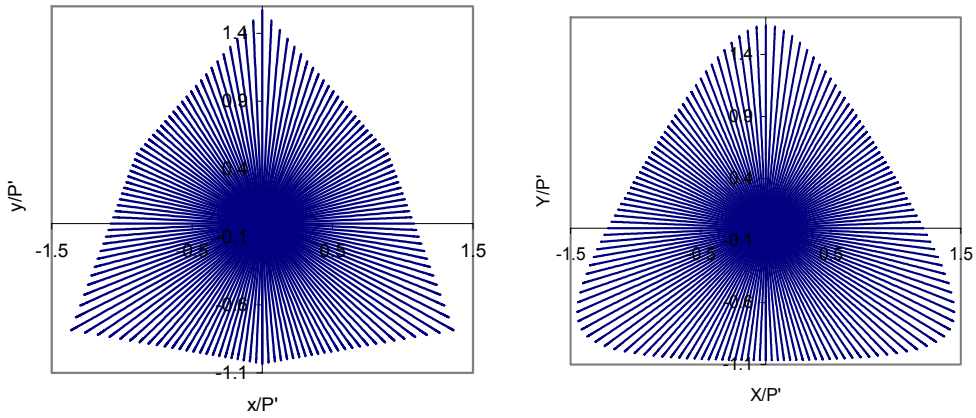


Figure 1.6: Stress path in a pi plane a) Plaxis liquefaction model (UBC3D), b) Hypoplasticity model

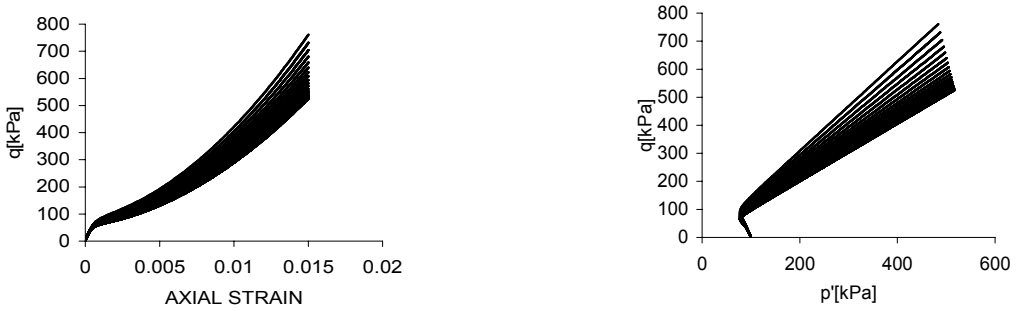


a) Plaxis Liquefaction model (UBC3D)

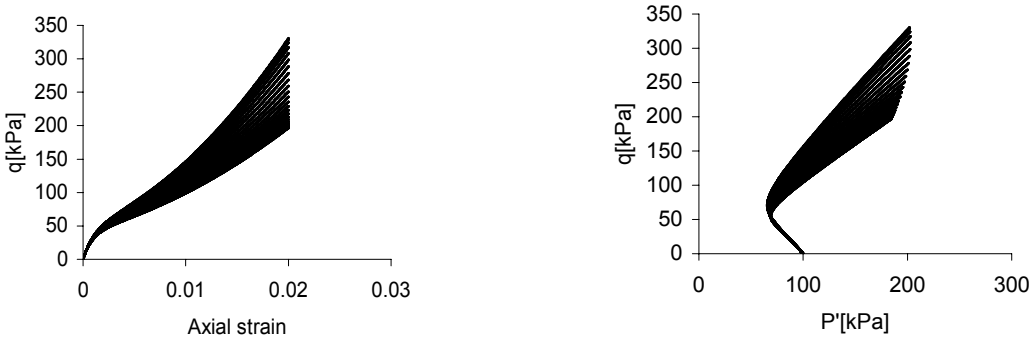


b) Hypoplasticity

Figure 1.7: stress –strain paths during monotonic isochoric deformation at various stress states (for radial strain increments in $\pi$ plane)

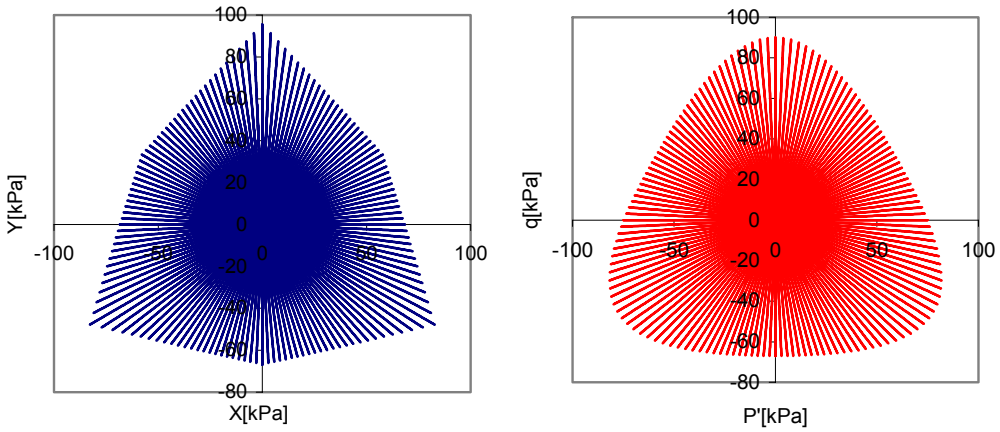


(a) (b)

Figure 1.8: Stress path in a $\pi$ plane a) Plaxis liquefaction model (UBC3D), b) Hypoplasticity model during isochoric cyclic deformation (radial cycles of strain in the $\pi$ plane)

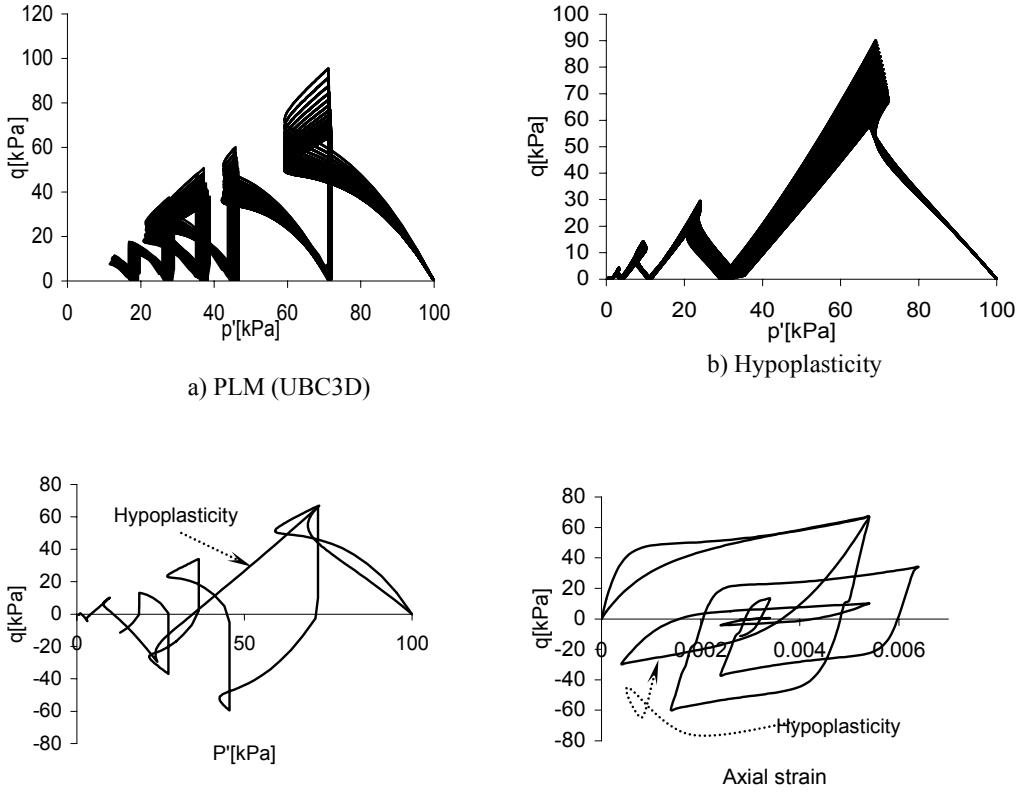


Figure 1.9: Comparison of stress-strain paths during isochoric cyclic deformation.

As shown in figures, the PLM (UBC3D) model shows a good agreement to mobilization of the stress path in the $\pi$ plane to the hypoplastic model during isochoric deformation (both cyclic and monotonic). Unloading plasticity is not considered in this version.

## 2.2 Element tests

The model is verified for various types of the conventional element tests. The numerical tests show the expected stress-strain paths under various conditions. The figures merely demonstrate the type of path in the said conditions.

Table 3: model parameters for the various runs

| parameter | 1 | 2 | 3 | 4 | 5 |
|---|---|---|---|---|---|
| $k_G^e$ | 400 | 800 | 200 | 600 | 600 |
| $k_B^e$ | 900 | 2000 | 400 | 400 | 400 |
| $k_G^p$ | 400 | 1200 | 100 | 600 | 800 |
| $ne$ | 0.5 | 0.5 | 0.5 | 0.5 | 0.5 |
| $me$ | 0.5 | 0.5 | 0.5 | 0.5 | 0.5 |
| $np$ | 0.5 | 0.5 | 0.5 | 0.5 | 0.5 |
| $\varphi_{cv}$ | 32 | 32 | 32 | 32 | 32 |
| $\varphi_p$ | 33 | 40 | 32 | 32 | 32,31 |
| $c$ | 0 | 0 | 0 | 0 | 0 |
| $R_f$ | 0.98 | 0.98 | 0.98 | 0.98 | 0.98 |
| $\sigma_t$ | 100 | 100 | 100 | 100 | 100 |

### 2.2.1 Oedometer test

As shown in Figure 1.11 Oedometer stress path can be predicted. However, due to absence of a cap, the prediction may not mach to experimental results. Since the aim of the liquefaction model is primarily to simulate the liquefaction behaviour of sand, adding a cap will not be an important issue.

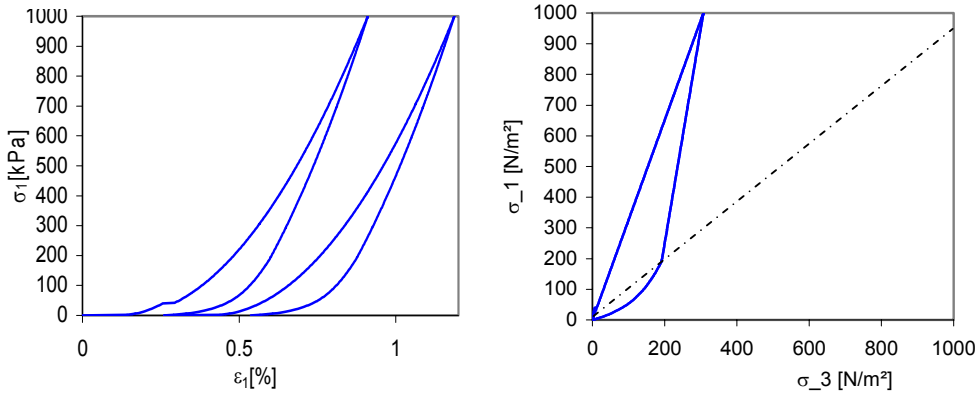


Figure 1.10: Oedometer stress – strain curve (model parameters, Table 3, column 4)

### 2.2.2 Triaxial Compression tests

The following figures show stress-strain paths of triaxial compression simulations under various conditions. The various simulations show the expected types of stress-strain, stress-stress paths under various conditions.

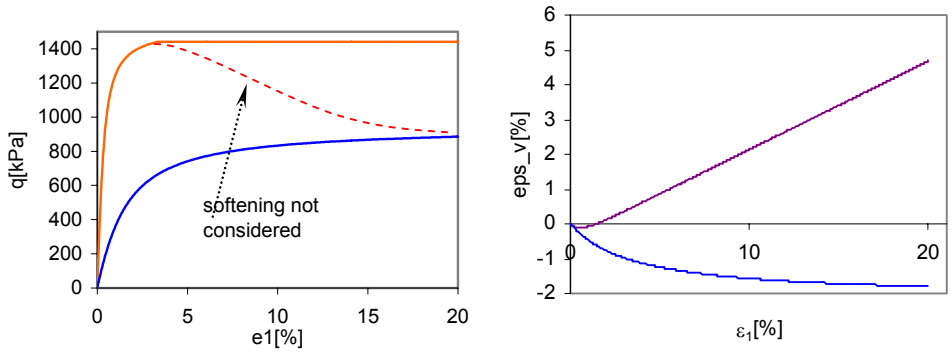


Figure1.11: Stress strain curves during drained triaxial compression simulations of dilative and contractive samples (Model parameters: for blue lines, table 3, column 3; for orange lines, table 3, column 2)

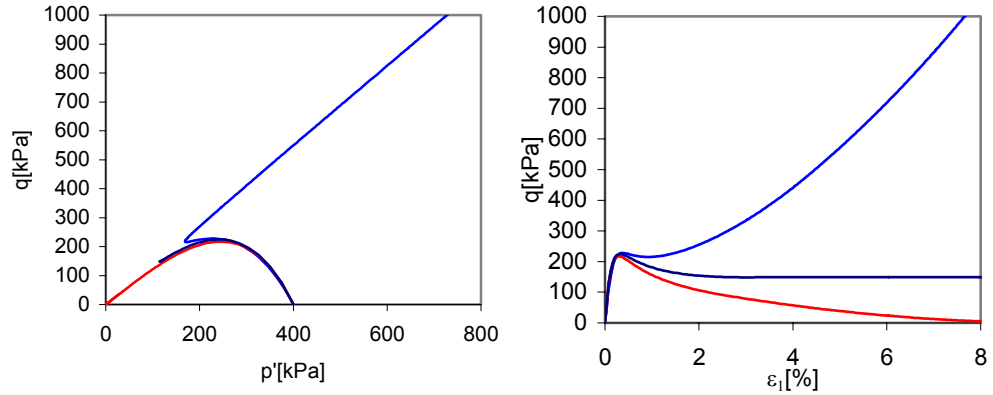


Figure1.12: Undrained simulations of dilative, contractive and very contractive samples (Model parameters: for blue lines, table 3, column 1; for orange lines, table 3, column 5 [Drak blue: $\varphi_p = 32^0$ red: $\varphi_p = 31^0$ )

### 2.2.3 Simple shear tests

Various simple shear tests are run in the Plaxis virtual lab tool. Both monotonic and cyclic simple shear simulations demonstrate the capability of the model to capture these types of soil responses. The type of pore pressure build up and effective stress path depict as obtained through various laboratory investigations.

#### 2.2.3.1 Drained and undrained monotonic simple shear tests

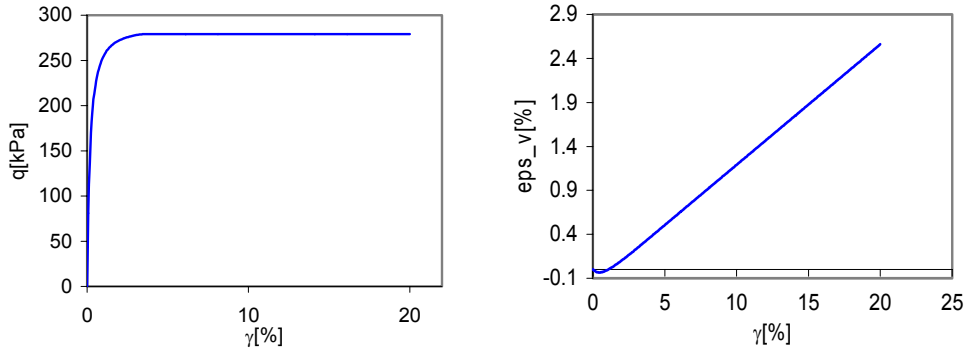


Figure 1.13: Drained simple shear simulation of a dilative sample (for orange lines, table 3, column 2)

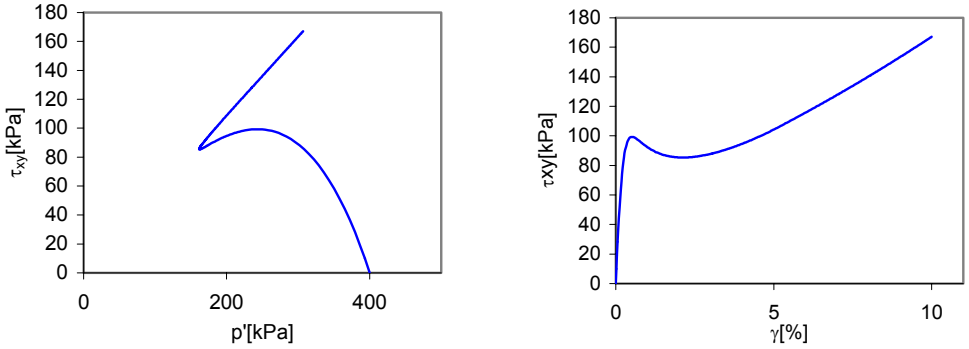


Figure 1.14: Undrained simple shear simulation of a dilative sample (Model parameters: for blue lines, table 3, column 1)

#### 2.2.3.2 Drained and undrained cyclic simple shear tests

The model can predict accumulations of volumetric strain during strain cycles of given amplitude. This has been introduced using a simple procedure of loading and unloading criterion by tracking the mobilized friction angle. This is also an important step towards modelling cyclic strain or stress induced liquefaction. Figure 1.16 shows the model response during application of cyclic simple shear under drained condition.

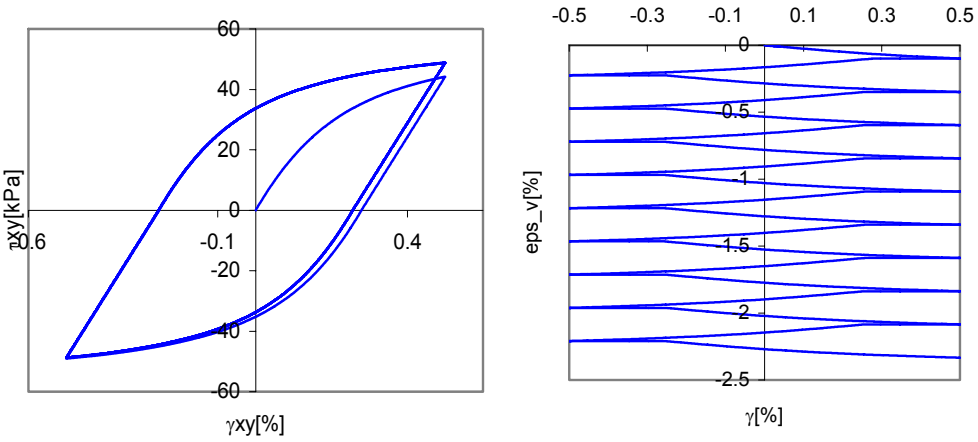


Figure 1.15: drained strain controlled cyclic simple shear response (Model parameters, table 3, and column 1)

The area of the loop in Figure 1.16 gives the energy dissipated. The area is expected to be more dissipative than would have been from test results. This is due to the simple unloading reloading criteria introduced in the model.

Although the model is applicable to the general behaviour of granular materials, our focus currently is on its applicability to model liquefaction behaviour of granular materials under various loading conditions. Figures demonstrate the applicability of the model for cyclic conditions.

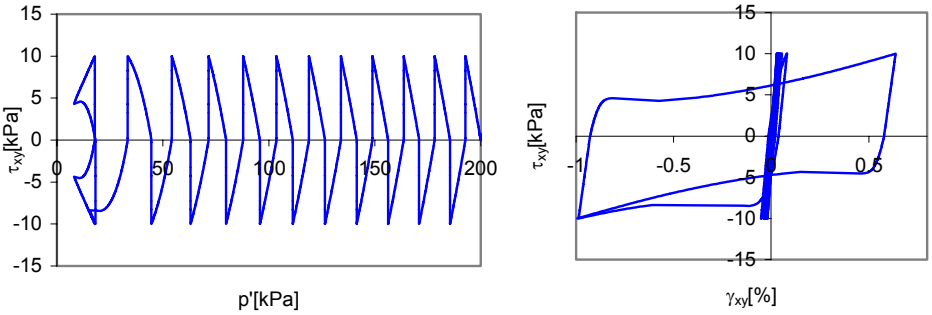


Figure 1.16: Model response during application of a constant shear stress cycles of 10kPa (Model parameters: table, column 1)

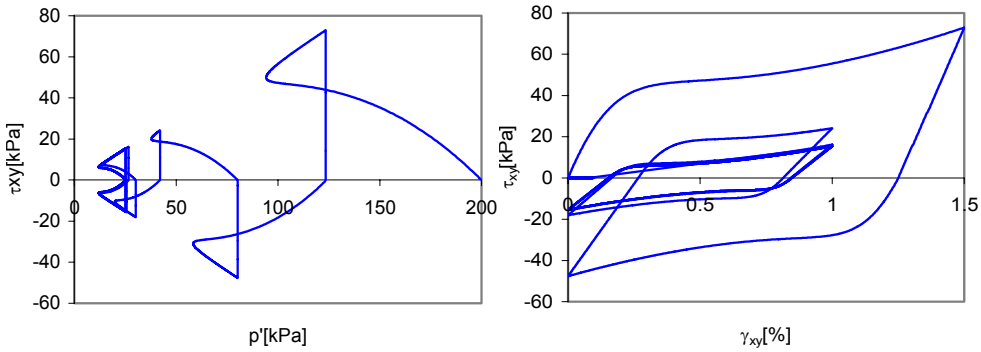


Figure 1.17: Model responses during application of a constant shear strain cycles (Model parameters: table, column 1, with peak friction angle $40^0$)

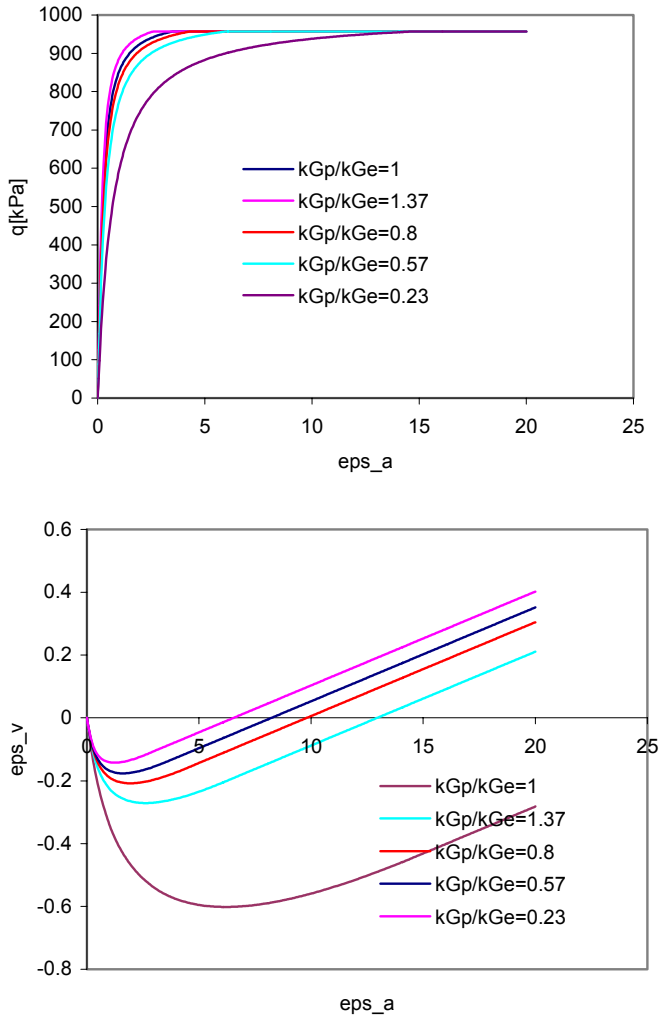


Figure 1.18: Influence of the parameter $k_G^p$

As shown in Figure 1.19, lower values of $k_G^p$ have a significant effect on the volumetric strain accumulation of the simulated results. Hence, this parameter requires special attention during simulation of liquefaction behaviour of sand. For contractive soils where liquefaction is expected, appropriate value of $k_G^p$ may be obtained from:

$$\frac{k_G^p}{k_B^e} = \frac{-72\eta \sin^2 \varphi_p}{\left((6+\eta)\sin\varphi_p - 3\eta R_f\right)^2} \frac{3\eta - (6+\eta)\sin\varphi_{cv}}{18 + (6+\eta)\sin\varphi_{cv}} \tag{22}$$

Where $k_B^e$ is the bulk modulus number, $\eta$ is the slope of the instability line, $\varphi_p$ is the peak friction angle, $\varphi_{cv}$ is the constant volume friction angle and $R_f$ is the failure ratio.

It should be also noted that direct relation is obtained for the ratio of the plastic shear modulus number to the elastic bulk modulus number considering a stress independent Poisson's ratio as.

$$\frac{k_G^e}{k_B^e} = 1.5\frac{1-2v}{1+v} \tag{23}$$

### 2.2.4 Validation of the model against triaxial stress state

Nerlerk Sand

From the data base of the Golder associates, the reported values of the slope of the critical state void ratio and the critical state void ratio are 0.049 and 0.849 respectively. Hence, assuming logarithmic relation with the mean normal pressure, the initial states of various samples is shown in Figure:

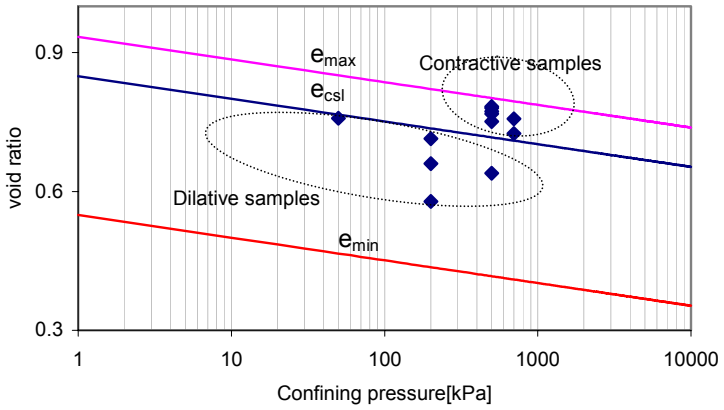

Figure 1.19: State of various Nerlerk sand samples considered relative to the critical state condition.

Table 4: summary of states of the various samples and critical state parameters of the Nerlerk sand

| $e_{max}$~1.1 $e_{cs0}$ | $e_{min}$ | $e_{cs0}$ | $\lambda_{cs}$ |
|---|---|---|---|
| 0.934 | 0.549 | 0.849 | 0.049 |

| Sample ID | $e_0$ | $p_0$ | $\Psi_0$ | RD | $\varphi_p$ |
|---|---|---|---|---|---|
| CID_G151 | 0.714 | 200 | -0.032 | 57.13 | 33 |
| CID_G154 | 0.758 | 50 | -0.008 | 45.70 | 34 |
| CID_G155 | 0.639 | 500 | -0.078 | 76.62 | 36 |
| CID_G156 | 0.66 | 200 | -0.076 | 71.16 | 36 |
| CID_G157 | 0.578 | 200 | -0.158 | 92.47 | 40 |
| CIU_G101 | 0.783 | 500 | 0.067 | 39.20 | eqn1.206 |
| CIU_G103 | 0.78 | 500 | 0.063 | 39.98 | eqn1.206 |
| CIU_G104 | 0.757 | 700 | 0.047 | 45.96 | eqn1.206 |
| CIU_G105 | 0.751 | 500 | 0.034 | 47.52 | eqn1.206 |
| CIU_G106 | 0.768 | 500 | 0.051 | 43.10 | eqn1.206 |
| CIU_G107 | 0.725 | 700 | 0.015 | 54.27 | eqn1.206 |
| CIU_G108 | 0.773 | 500 | 0.056 | 41.80 | eqn1.206 |

Peak friction angle:

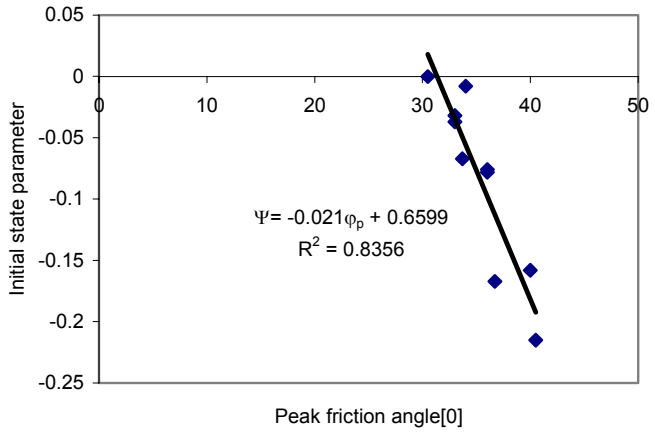


Figure 1.20: Correlation between initial state parameter and peak friction angle for Nerlerk sand

The peak friction angle is correlated with the initial state parameter according to:

$$\varphi_p \approx 31^0 - 47\Psi_0 \qquad (1.24)$$

For very contractive samples, equation (1.24) gives a peak friction angle slightly lower than the critical state friction angle. From theoretical point of view, the peak should rather be the critical state friction angle. However, the model behaviour of very contractive soils supports slightly lower peak friction angle value. The critical state friction angle is about $30.5^0$.

Table 5: estimated state dependent model parameters

| Sample ID | RD | $\varphi_p$ | $k_G^e$ | $K_B^e$ | $k_B^p$ |
|---|---|---|---|---|---|
| CID_G151 | 57.13 | 33 | 419 | 909 | 282 |
| CID_G154 | 45.70 | 34 | 393 | 853 | 234 |
| CID_G155 | 76.62 | 36 | 464 | 1,006 | 379 |
| CID_G156 | 71.16 | 36 | 446 | 968 | 346 |
| CID_G157 | 92.47 | 40 | 485 | 1,051 | 456 |
| CIU_G101 | 39.20 | 28 | 403 | 875 | 219 |
| CIU_G103 | 39.98 | 28 | 404 | 876 | 221 |
| CIU_G104 | 45.96 | 29 | 416 | 902 | 245 |
| CIU_G105 | 47.52 | 30 | 416 | 901 | 250 |
| CIU_G106 | 43.10 | 29 | 409 | 887 | 233 |
| CIU_G107 | 54.27 | 31 | 429 | 931 | 279 |
| CIU_G108 | 41.80 | 29 | 407 | 882 | 228 |

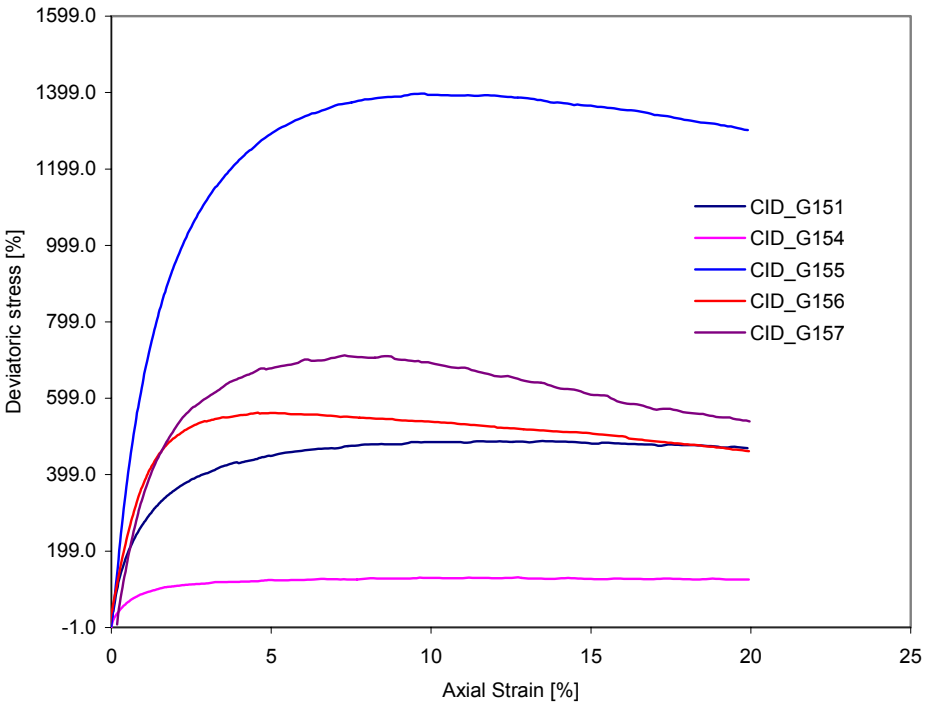


Figure 1.21: Plots of deviatoric stress versus axial strain from test results on the Nerlerk sand [data base of Golder Associates]

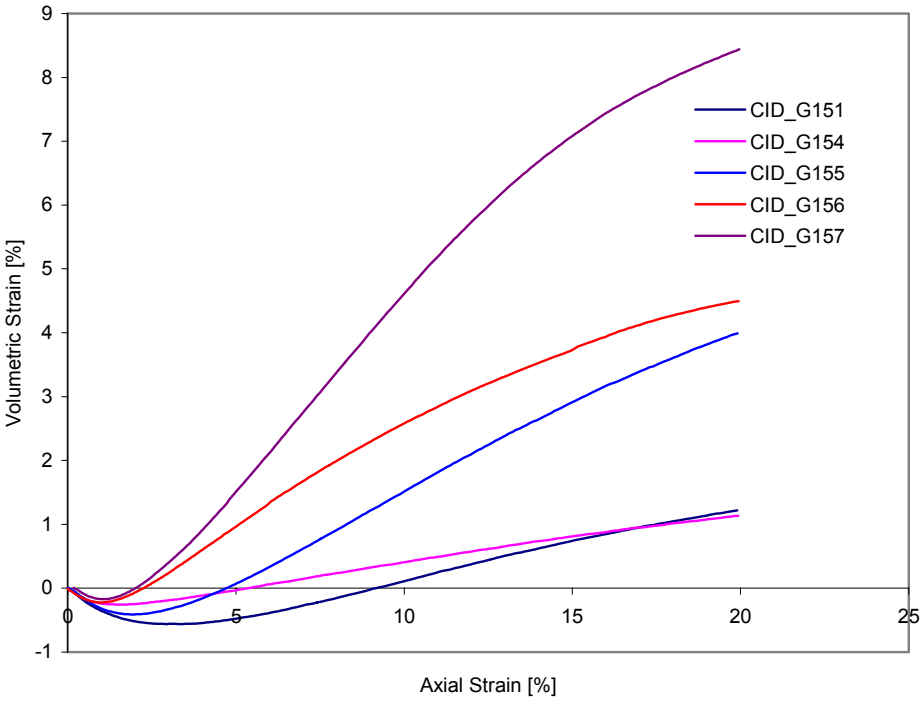


Figure 1.22: Plots of volumetric strain versus axial strain from test results on the Nerlerk sand [data base of Golder Associates]

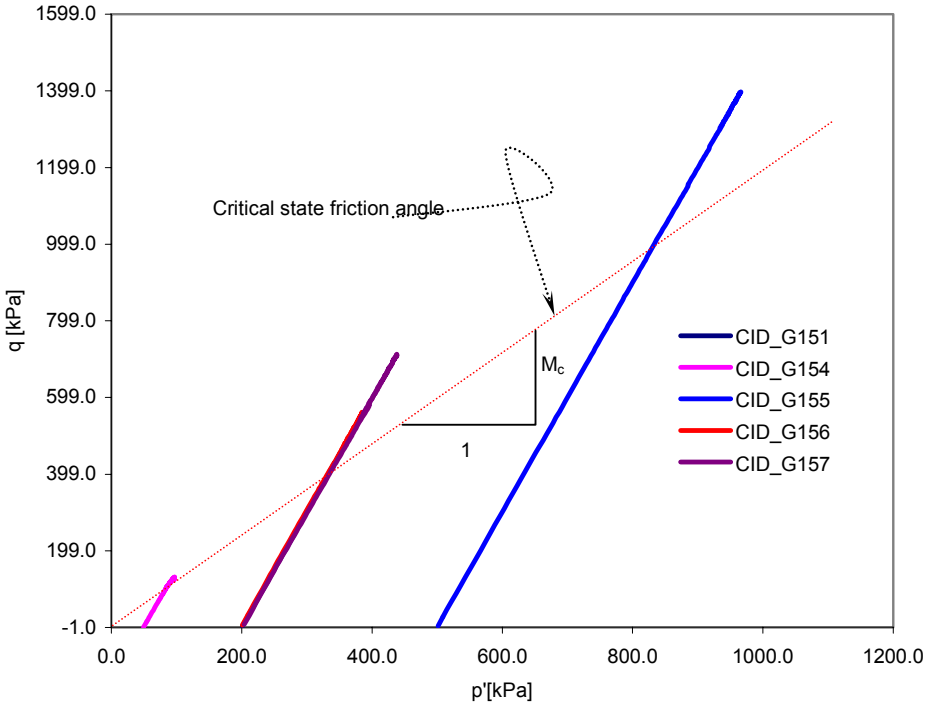


Figure 1.23: Plots of deviatoric stress versus mean normal stress from test results on the Nerlerk sand [data base of Golder Associates]

Model response during drained simulations of the Nerlerk sand

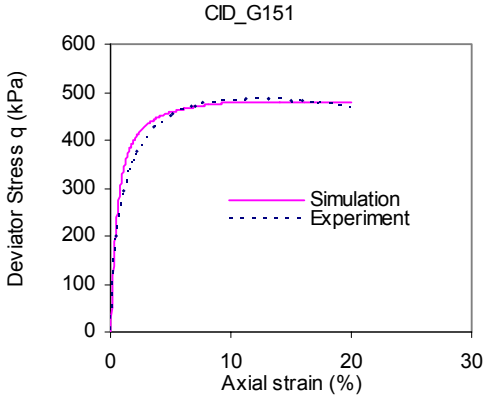


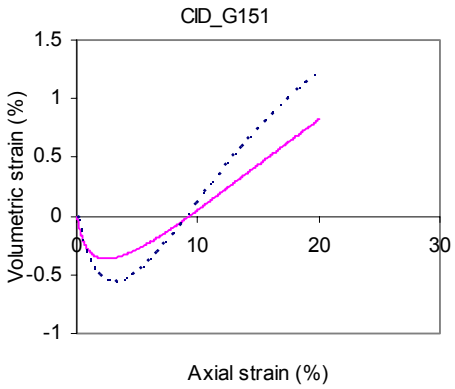


Confining stress 200kPa

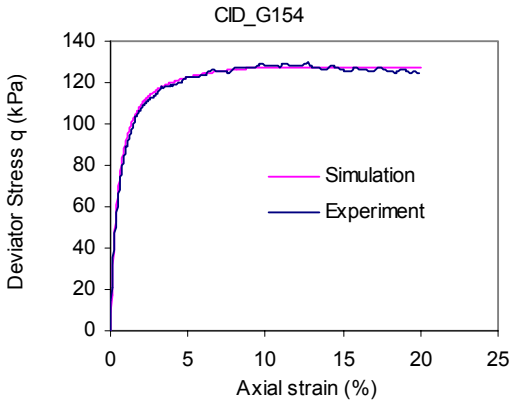


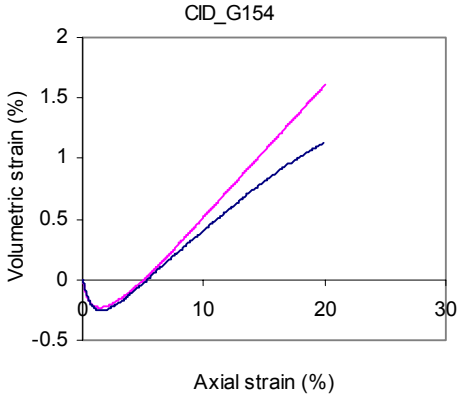


Confining stress 50kPa

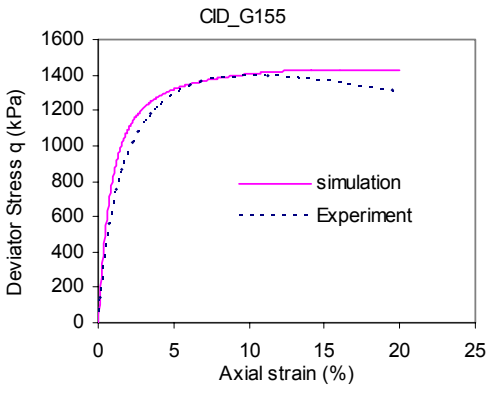


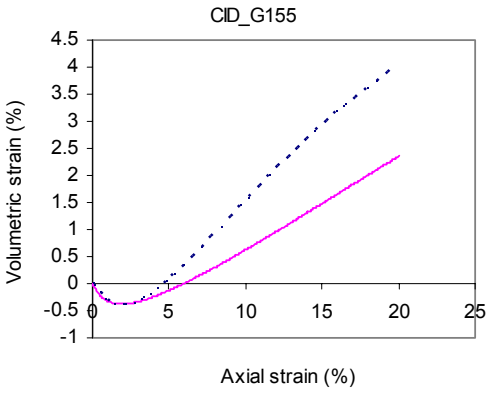


Confining stress 500kPa

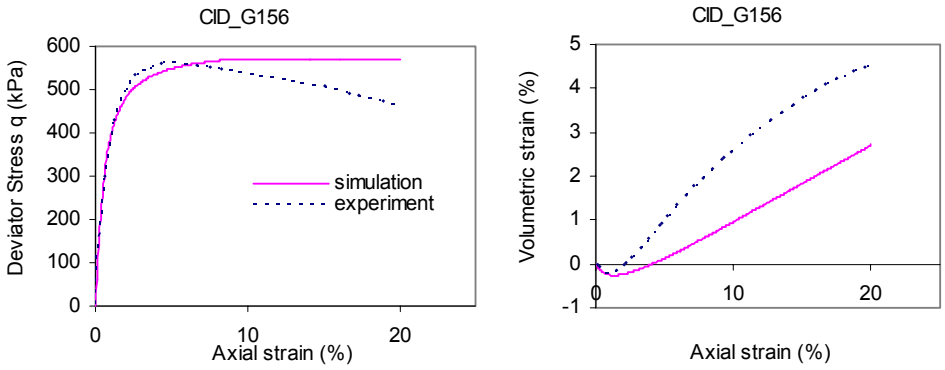


Confining stress 200 kPa

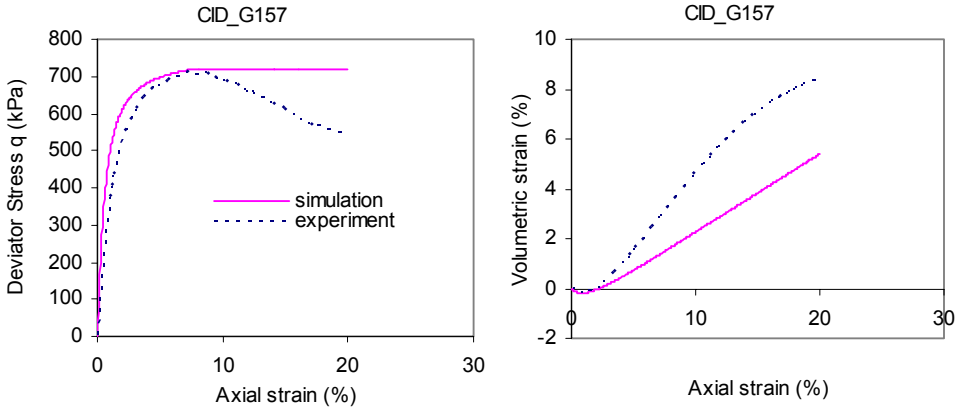


Undrained

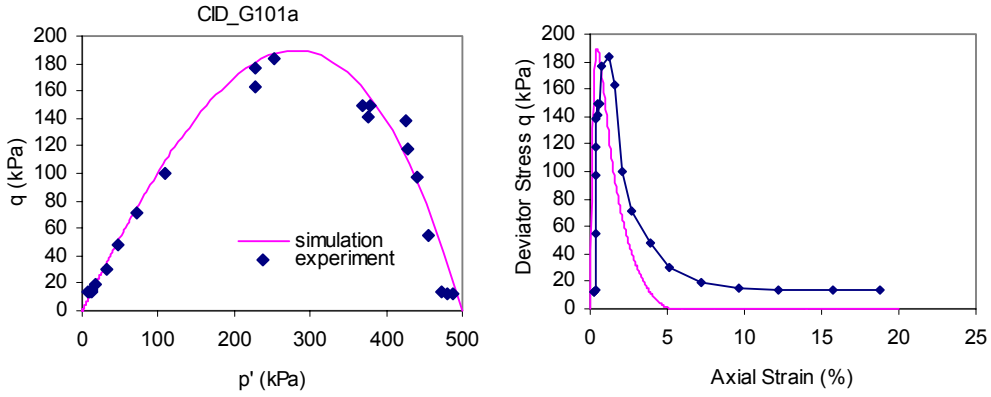


Confining pressure 500kPa

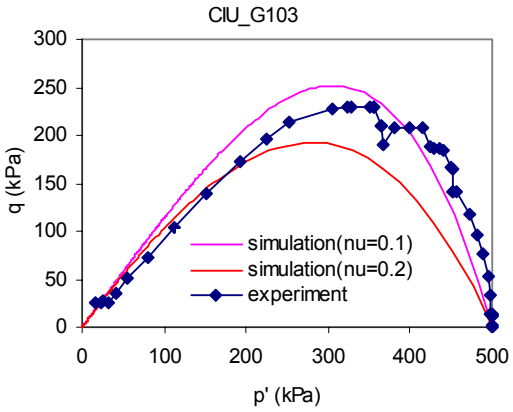


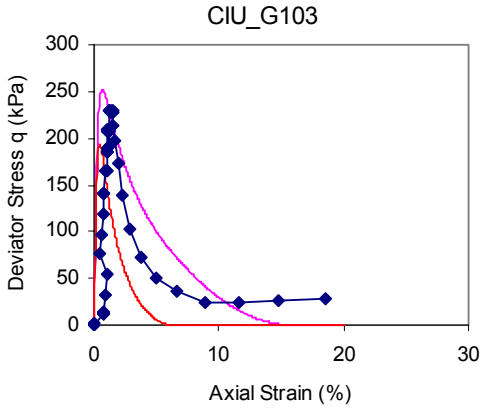


Confining pressure 500kPa

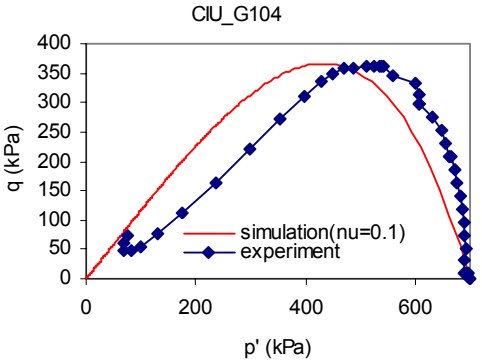


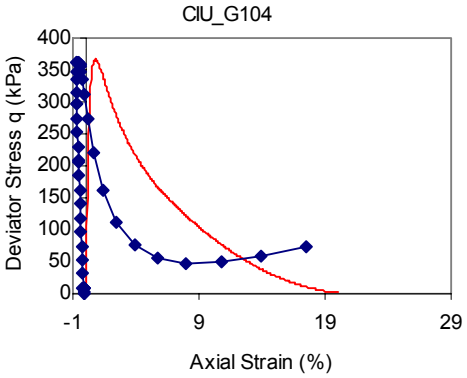


Confining pressure 700kPa

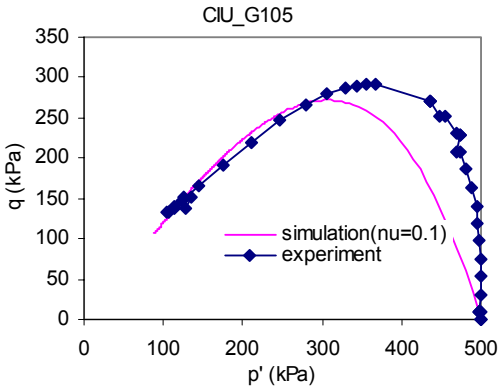


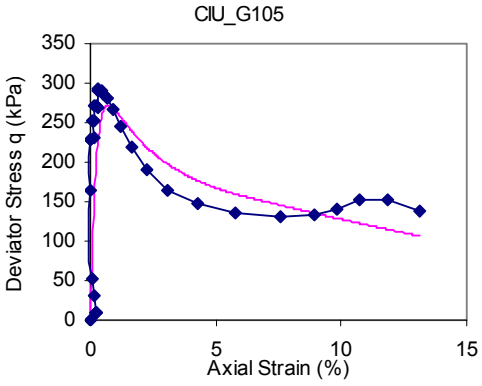


Confining pressure 500kPa

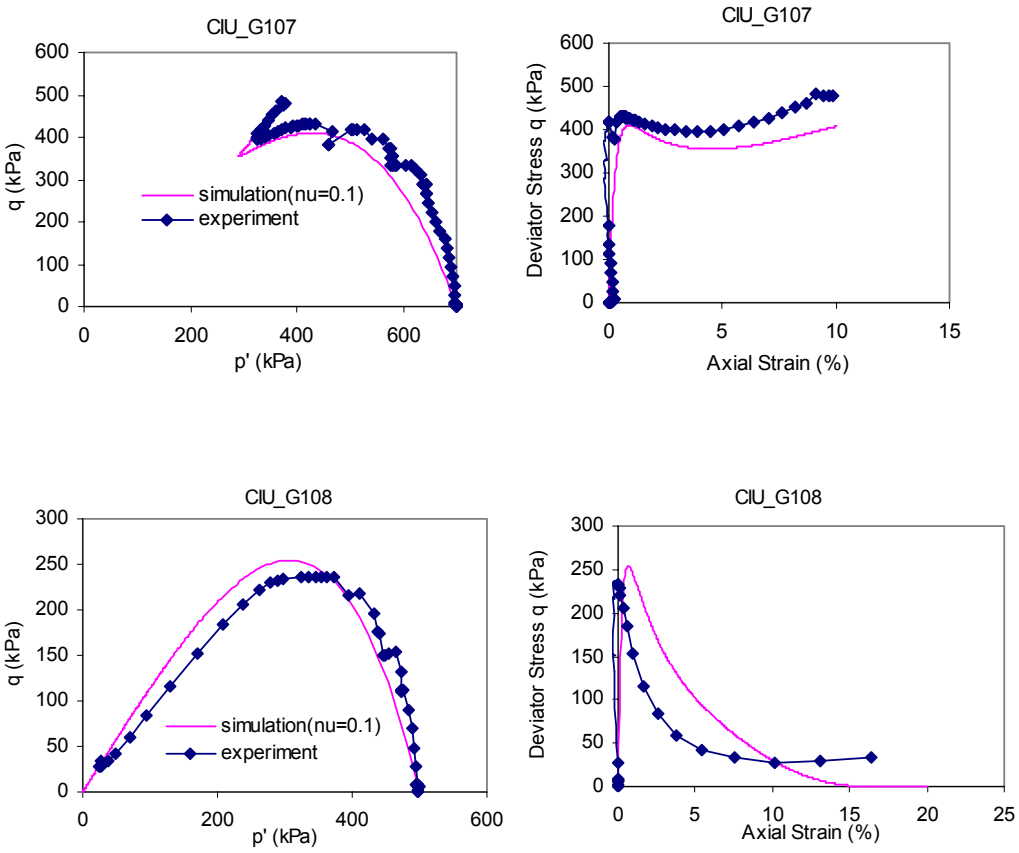


Confining pressure 500kPa

Drained simulations show a good agreement until the phase transformation. Beyond the phase transformation point, volumetric accumulation due to dilatancy is lower than seen in the experiments. This is partially due to the flow rule used in this model. As compared to the original Rowe's stress dilatancy formulation, the stress dilatancy formulation used by Byrne, et al under predicts the volumetric strain accumulation beyond the phase transformation line.

### 2.2.5 Boundary Value Problems

Thus far various element tests demonstrated that the model captures essential behaviours of granular materials in both drained and undrained flow boundary conditions. In this section, we shall demonstrate the general applicability of the model in a finite element scheme.

1. Shear wave under a soil column (Centrifuge test 1)

The following figure shows a uniform horizontal sand layer of thickness 37m. A base motion of 50 cycles of 0.2g acceleration at a frequency of 1.5Hz is applied. An initial $k0$ value of 0.5 is considered.

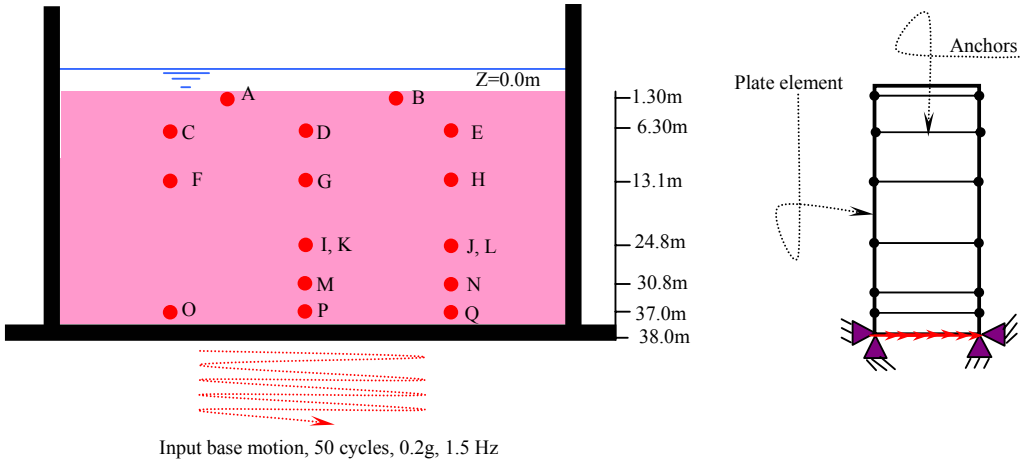


a) Set up b) Schematization

Figure 1.24: Simulation of centrifuge test on a soil column

The time history of the base acceleration is therefore given as:

$$a = 0.2g\sin\left(2\pi ft\right) \tag{25}$$

where $f$ is the frequency and $g$ is the acceleration of gravity.

Table 6: parameters used in the model

| Layer | $\varphi_{cv}$ | $\varphi_p$ | $k_G^e$ | $k_B^e$ | $k_G^p$ | Others |
|---|---|---|---|---|---|---|
| 1 | 31 | 32 | 1200 | 1000 | 2500 | Default value (see table) |

The following results are generally reported at the end of the calculation phase (30 dynamic seconds).

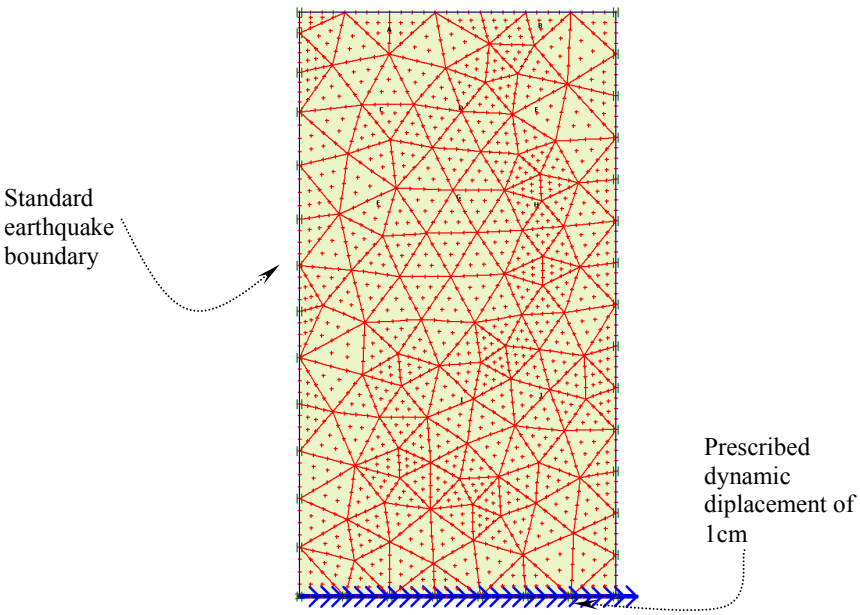


Figure 1.25: Plaxis finite element mesh: Number of elements 201, number of nodes 1961, number of stress points, 2412, average size 1.92m

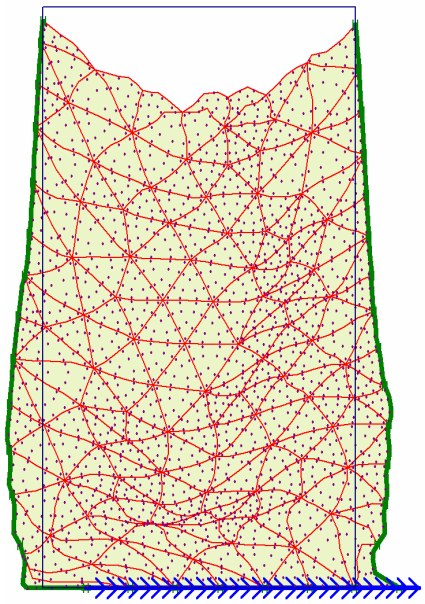

Figure 1.26: Deformed mesh (scaled 10 times) at the end of 30 dynamic seconds. Total displacement (extreme value 67cm)

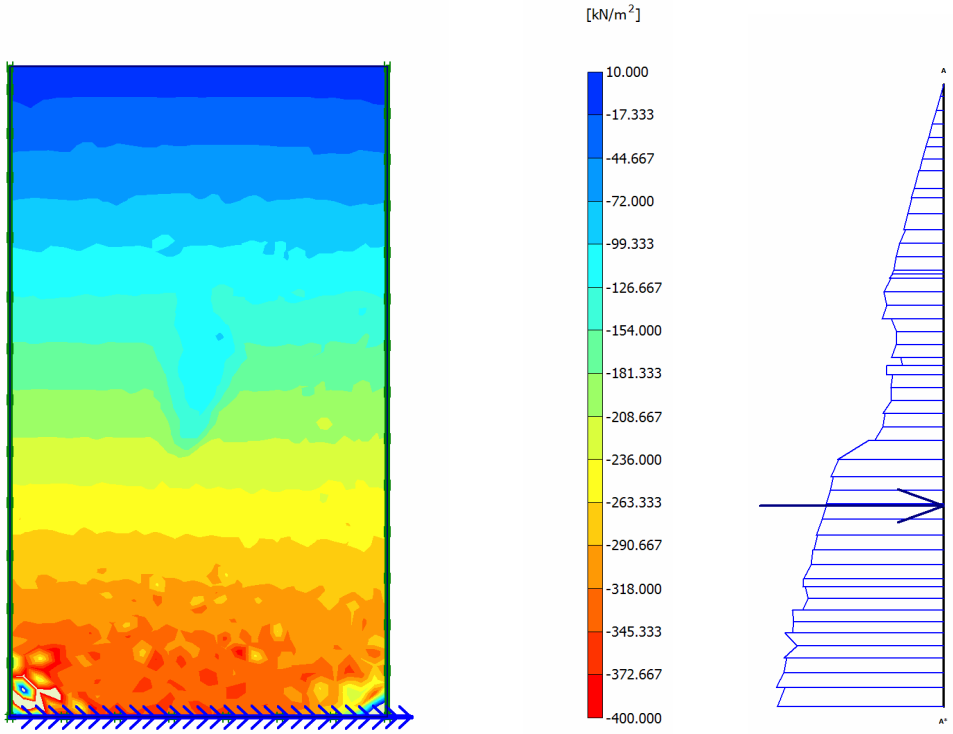


Figure 1.27: Excess pore pressure profile at the end of the calculation phase

As seen in figure, the pore pressure develops to the extent of the vertical stress along the profile. This shows the near liquefaction (liquefaction phenomena). Various plots at selected points demonstrate the capability of the model to capture pore pressure accumulation in dynamic calculations leading to liquefaction.

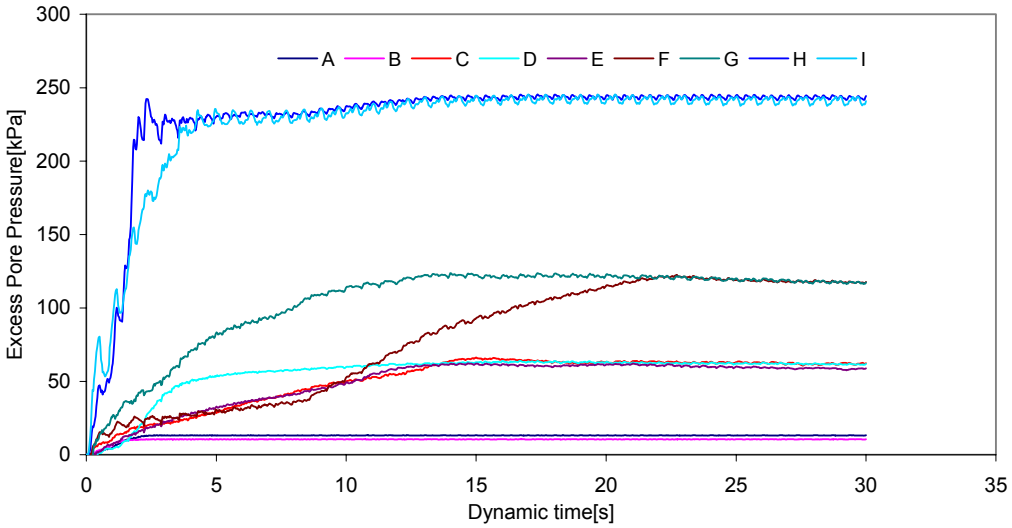


Figure 1.28: Excess pore pressure development at various points along the profle

The significant loss of shear strength as a result of the very high excess pore pressure is shown in the following graphs at sample points.

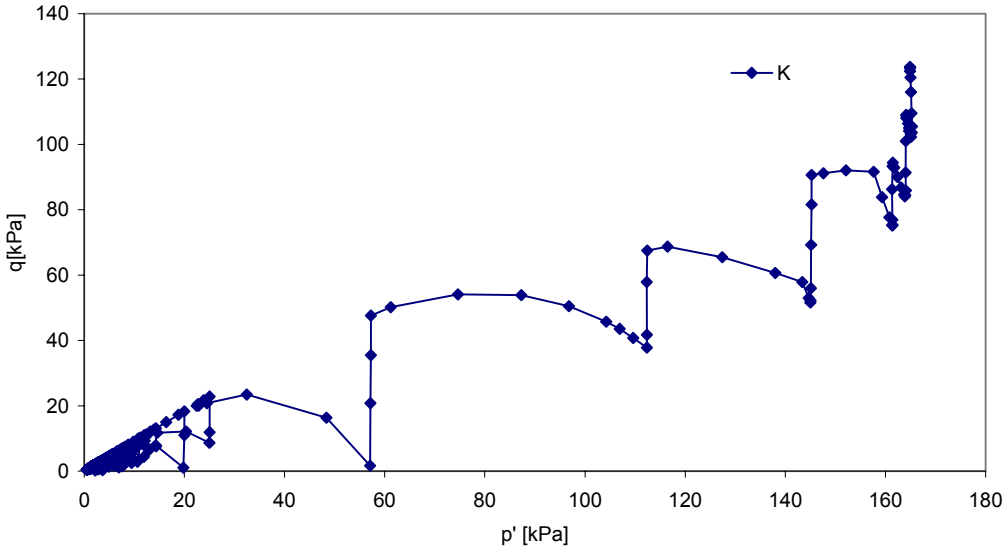


Figure 1.29: effective isotropic stress versus shear strength at point K

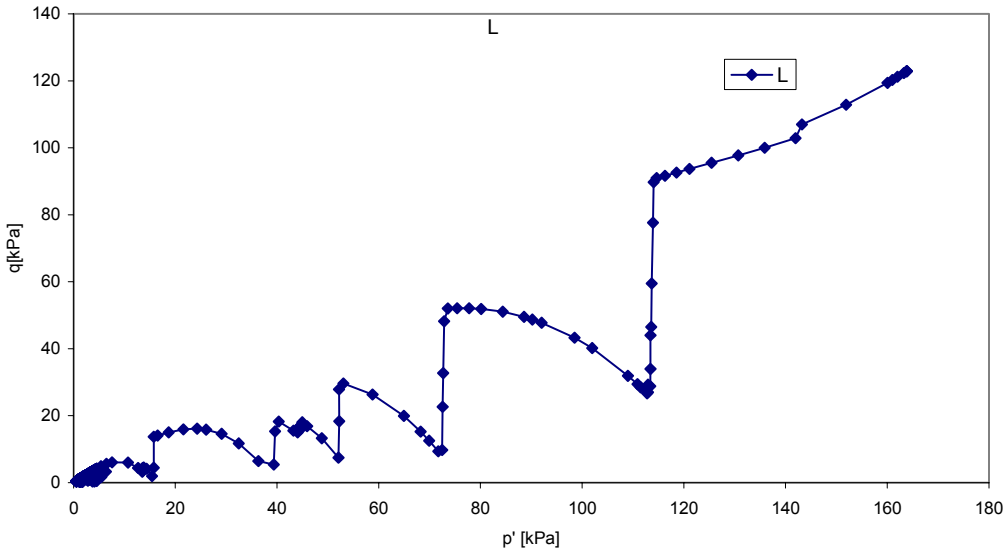


Figure 1.30: effective isotropic stress versus shear strength at point L

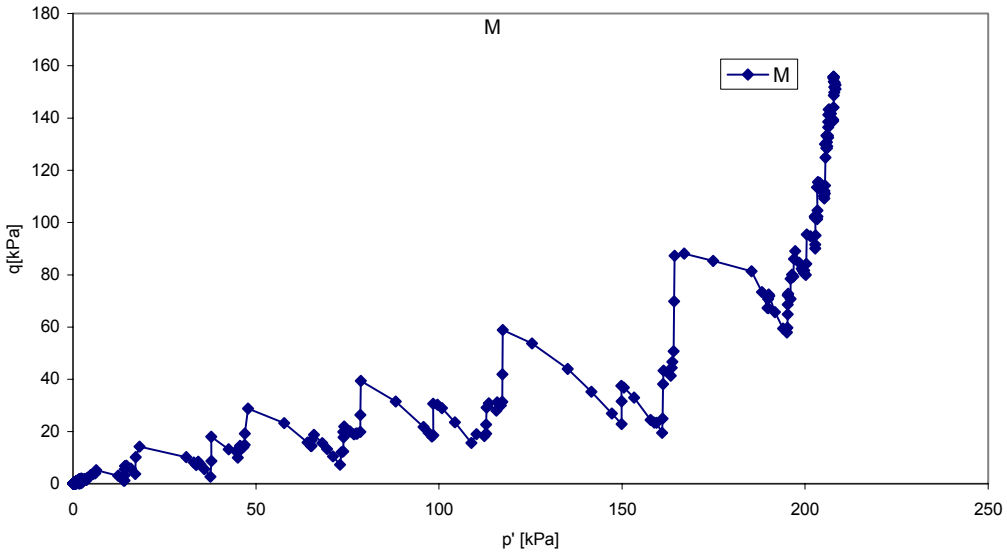


Figure 1.31: effective isotropic stress versus shear strength at point M

The start of the stress path is defined by a $k_0$ value of 0.5. In each acceleration cycle, the effective confining stress decreases by the amount of the excess pore pressure per cycle.

2. Shear wave under embankment (centrifuge test 2)

The dam cross-section shown in Figure 1.33 is used for further verification of application of the model for earthquake induced liquefaction analysis. A bed shake with 0.2g of 20cycles of frequency 1Hz represent a dynamic ground shaking similar to an earthquake.

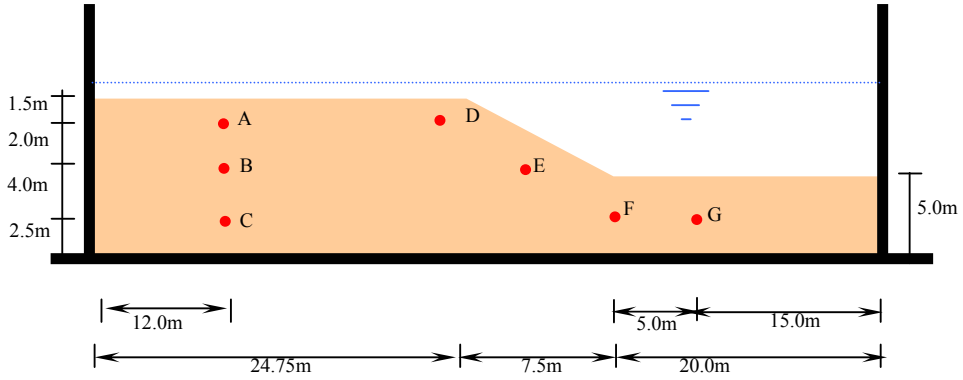


Figure 1. 32: Dam cross-section detail and points of LVDT measurement

For modelling, the rigid walls both the base and the vertical sides can be considered at the same relative position to each other during the shaking (Byrne, et al).

Table 7: model parameters

| Layer | $\varphi_{cv}$ | $\varphi_p$ | $k_G^e$ | $k_B^e$ | $k_G^p$ | Others |
|---|---|---|---|---|---|---|
| 1 | $34.4^0$ | $35^0$ | 1000 | 800 | 1000 | Default value (see table) |

Calculation phases

Phase 1. Excavate the lower portion
Phase 2. Apply dynamic displacement of 0.01m
Phase 3. Apply acceleration multiplier from input file.

The following results are generated at the end of the phase (only sample results are shown).

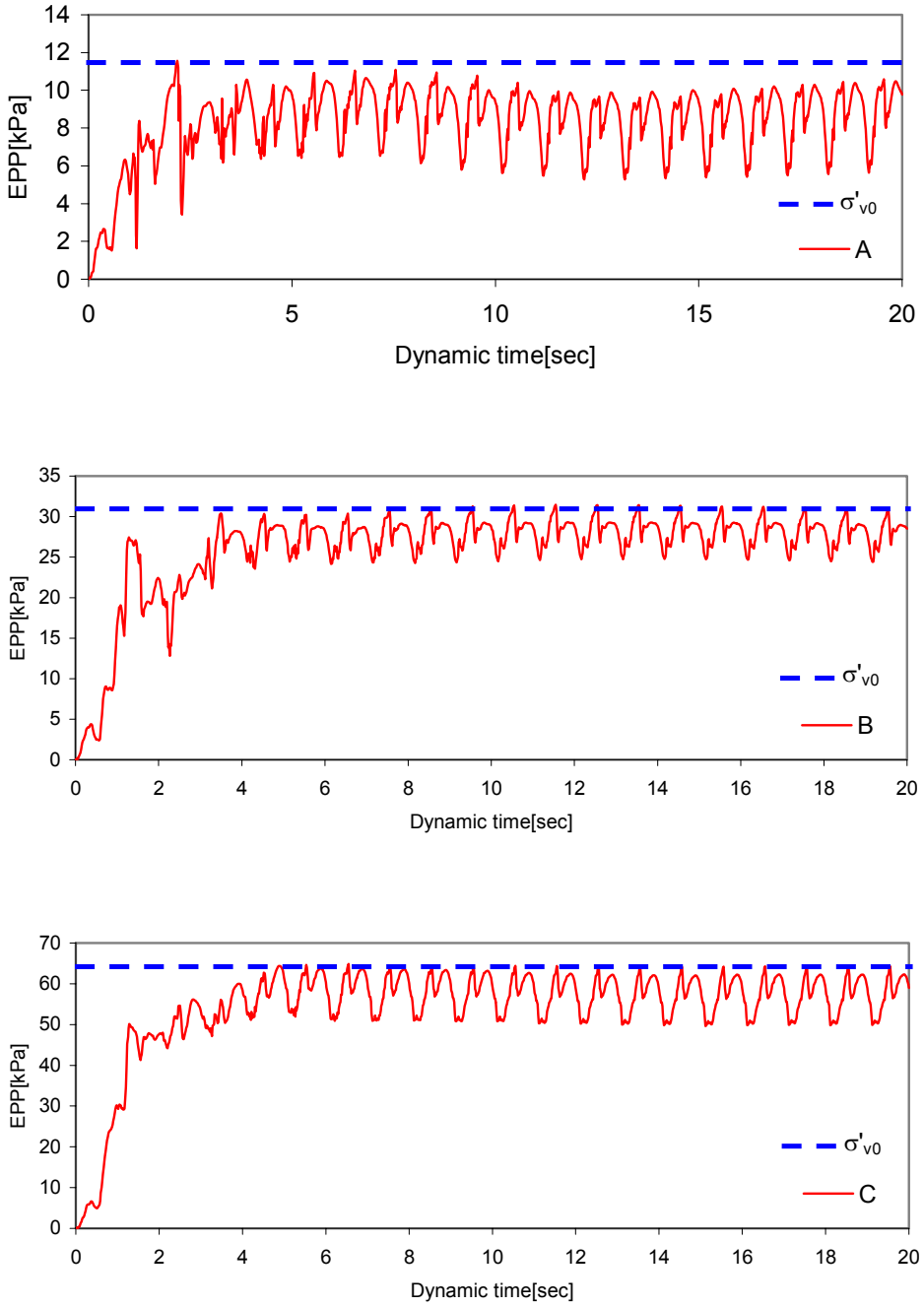


Figure 1. 33: Pore pressure accumulation during the cyclic loading PLM (UBC3D)

For these points (A , B and C- pp6, pp5 and pp1 respectively as denoted in the following figures) the results of the UBC2D model and experimental results are shown.

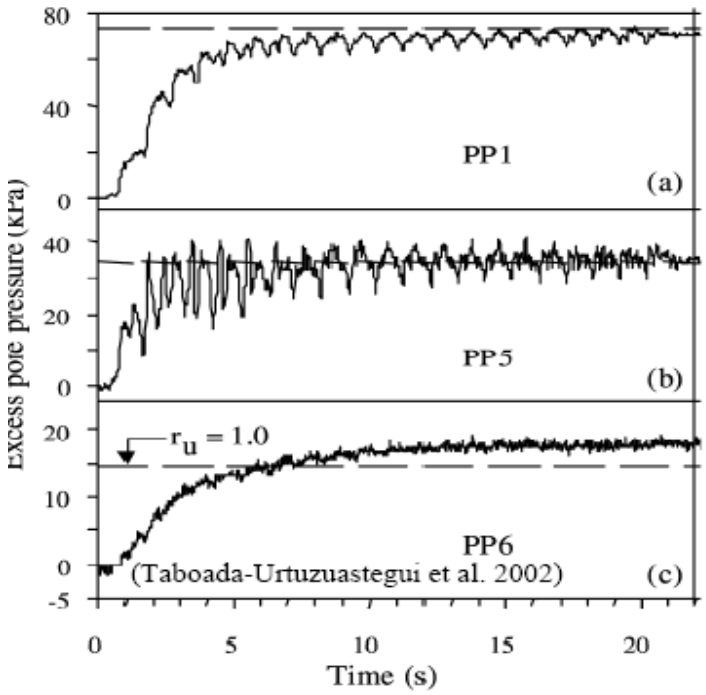


a)

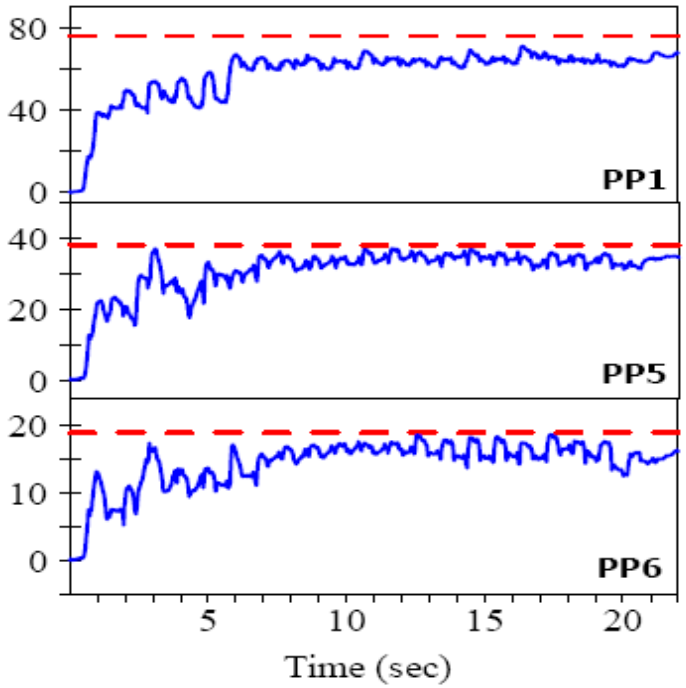


b)

Figure 1. 34: Pore pressure accumulation during cyclic loading a) Experimental results and b) model runs using UBC2D (Byrne, etal)

As demonstrated in Figure 1-34, the PLM (UBC3D) model is capable of predicting pore pressure accumulation during cyclic loading.

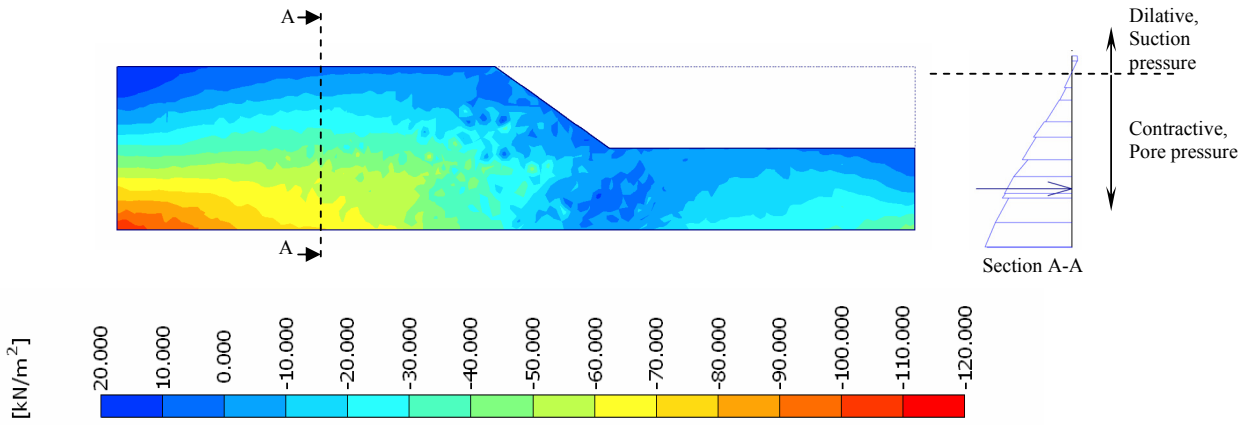


Figure 1. 35: Excess pore pressure profile at the end of the 20 cycles.

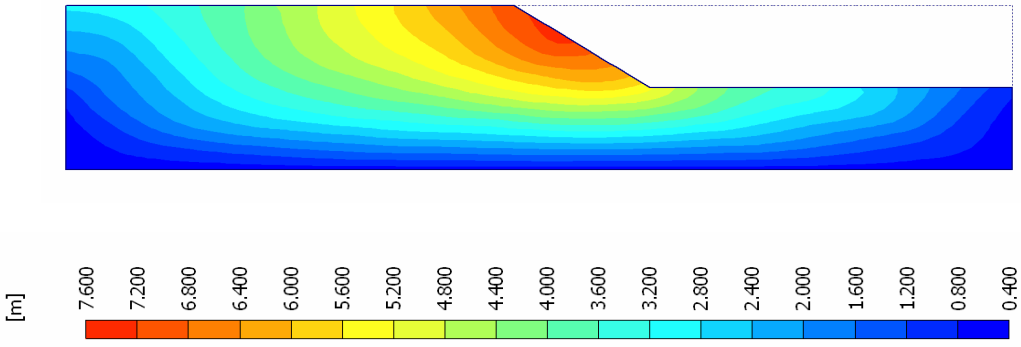


Figure 1. 36: Total displacement at the end of the 20 cycles (extreme total displacement about 7.3m).